HARVARD UNIVERSITY

Graduate School of Arts and Sciences

DISSERTATION ACCEPTANCE CERTIFICATE

The undersigned, appointed by the

Harvard John A. Paulson School of Engineering and Applied Sciences
have examined a dissertation entitled:

"From Rings to Smoke: the quest to uncover a mechanism of turbulence"

presented by: Ryan Roberts McKeown

candidate for the degree of Doctor of Philosophy and here by
certify that it is worthy of acceptance.

Signature _____

Typed name: Professor S. Rubinstein

Signature _____

Typed name: Professor M. Brenner

Signature _____

Typed name: Professor D. Nelson

April 16, 2020

From Rings to Smoke: the quest to uncover a mechanism of turbulence

Thesis advisor: Professor Shmuel M. Rubinstein   Ryan Roberts McKeown

From Rings to Smoke: the quest to uncover a mechanism of turbulence

ABSTRACT

The equations of motion that govern the dynamics of fluid flows–the Navier-Stokes equations–were formulated nearly two centuries ago. In that time, we have made immense advancements in the ways that we understand these equations in order to characterize, analyze, and model a myriad of fluid flows. To this day, however, our understanding of how turbulent flows evolve dynamically remains limited. The challenge in understanding how turbulent flows develop arises from the complexity of the transfer of energy through the interactions of vortices over a broad range of length and time scales. These ubiquitous flows are notoriously difficult to study due to our lack of a mechanistic framework that encapsulates how vortices interact, break down, and form new generations of vortices, driving the cascade of energy down to the dissipative scale. Here we examine the violent, head-on collision of vortex rings in order to identify how the vortices break down into a transient turbulent flow. At moderate Reynolds numbers, the colliding vortices locally flatten each other and split into new, smaller generations of vortex filaments. These secondary filaments, themselves, interact with each other, flatten, and break down again in an iterative manner that is consistent with recent theoretical predictions. At higher Reynolds numbers, the colliding vortices generate a new ordered array of antiparallel secondary filaments through the onset of the elliptical instability. These secondary filaments interact, leading to the formation of even smaller tertiary filaments in the same manner as the preceding generation. We examine what role these vortex interactions play in the cascading of energy down to smaller scales in recent numerical studies of turbulence. This mechanistic framework could help shift the paradigm of viewing turbulence as a cascade of discrete instabilities through vortex interactions, rather than statistically.

Contents

Listing of figures

To my family and teachers: I never would have made it this far without your guidance, love, and support.

"If I have seen further, it is by standing on the shoulders of Giants."
  - Isaac Newton

Acknowledgments

This PhD has been one of the most exciting, challenging, fulfilling, at times infuriating yet most rewarding endeavour of my life. I came to Harvard knowing how to answer questions, and now I'm leaving with the wisdom of knowing to ask them; specifically, how to ask the right questions.

I would like to first thank my parents who instilled within me my work ethic, my determination, and the importance of education. I am so grateful for the sacrifices that my parents made to provide me with a better life than they had. I recently looked back at all the old family photos that I have, and it is clear that my parents are happiest at my and my siblings' graduations because nothing makes them happier than helping their children pursue their dreams. Mom and Dad, you taught me that I am capable of learning anything.

I thank my siblings–Chris, Sean, and Paige–and my Uncle John for your humor and for always giving me a hard time. Rest assured, I'll never get too full of myself with you all nearby.

I want to thank Rodolfo Ostilla-Mónico, Alain Pumir, and Michael Brenner for being the finest group of collaborators that I could ever ask for. Working with you all over the years has made me feel like no obstacle is insurmountable. Your guidance and mentorship have been a privilege.

I would like to also thank the National Science Foundation for funding my research through the Division of Mathematical Sciences and the Harvard Materials Research Science and Engineering Center.

I thank the members of the SMR Lab for being my second family in graduate school. Like the rest of my family, you all know how to make me laugh, how to give me a hard time, and how to always remind me–in our own dysfunctional way–that you're always looking out for me. Lisa, you are one of the kindest, most selfless people I've had the good fortune of working with, and I'm so grateful that I had you by my side throughout grad school and beyond. Will, thank you for being the older brother I never wanted but definitely needed in grad school. Sam, throughout our time in grad school, whether it was in lab, in the classroom, or just goofing around, thank you for always embracing "yes, and" with me; you're a true friend.

Lastly, Shmuel: my advisor, my mentor, and my boss. Thank you for teaching me how to ask questions (the right questions), how to do cutting-edge scientific research at a world-class level, and how to become a mentor to others. I am eternally grateful for the time that I've had to learn from you.

0
Introduction

When I first began my undergraduate education in engineering, I was under the impression that all of classical mechanics had been largely figured out. While new, transformative developments were emerging constantly in fields like biology, electronics, quantum mechanics, and astrophysics, there were no deep, open questions that remained about the interactions of everyday objects. The fundamental equations of motion governing such classical systems were established centuries ago by Newtonian mechanics and other conservation laws regarding how mechanical systems–discrete

or continuous–respond to external forcing. However, upon taking my first class in fluid mechanics, I quickly became aware of the main void remaining within our understanding of classical physics: turbulent flows.

Needless to say, this was shocking to learn. Surely, the physics of how incompressible fluids move and interact with other rigid bodies had been established and could be modelled and predicted. This is true under certain cases, namely laminar flows–when fluid elements flow in ordered parallel streamlines without mixing. Flows remain laminar when the viscous forces between fluid elements temper the inertial forces that drive them, thereby keeping the flow stable. However, when the inertial forces of a flow are so high that they overpower the viscous forces, the streamlines become unstable and the flow breaks down into a disordered ensemble of swirling eddies, known as turbulence. This transition to turbulence was first examined experimentally by Osborne Reynolds in 1883, who developed a dimensionless measure of this balance between inertial and viscous forces in a flow, eponymously known as the Reynolds number, Re:[61]

$$\text{Re} = \frac{\text{inertial forces}}{\text{viscous forces}} = \frac{UL}{\nu} \tag{1}$$

In this equation, U is the characteristic velocity scale of a flow, L is a characteristic length scale in a flow, and ν is the kinematic viscosity of the fluid. Though Reynolds initially proposed this dimensionless parameter for water flowing through a pipe, where U was the mean velocity of the flow and L was the diameter of the pipe, it has been applied over a myriad of different flow configurations. In each case, a flow will transition to a turbulent state when the Reynolds number reaches a threshold value, wherein the inertial behavior of the flow dominates. The applicability and extensibility of this dimensionless parameter in any incompressible flow demonstrates the universal nature of turbulence.

Turbulent flows are ubiquitous in everyday life, from the flows of streams, rivers, and oceans,

to the flows past moving cars and planes. The velocity fields of turbulent flows are disordered and irregular, meaning that they fluctuate both spatially and temporally. This is a consequence of the formation and interaction of eddies over a wide range of scales, from the largest scales where energy is injected into the flow, down to the smallest scales where it is dissipated through viscosity. The complicated nature of these dynamics has limited our understanding of how turbulence evolves on a fundamental level.

Our understanding of how the dynamics of viscous fluid flows evolve was developed in the early 1800s with the derivation and later formalization of the Navier-Stokes equations, shown in Eqs. (2) and (3)[12]. They characterize the equations of motion of an incompressible, Newtonian fluid with density, ρ and kinematic viscosity, ν.

$$\frac{\partial \mathbf{u}}{\partial t} + (\mathbf{u} \cdot \nabla) \mathbf{u} = -\frac{1}{\rho}\nabla p + \mathbf{f} + \nu \nabla^2 \mathbf{u} \tag{2}$$

$$\nabla \cdot \mathbf{u} = 0 \tag{3}$$

In these equations, $\mathbf{u}(x, y, z, t)$ is the velocity field of the flow, $p(x, y, z, t)$ is the pressure distribution, and $\mathbf{f}(x, y, z, t)$ is an external body force acting on the fluid. Eq. (2) represents the application of Newton's second law of motion in a continuum fluid model, whereby the momentum of each fluid element (the left side of the equation) is balanced by the forces acting on each fluid element (the right side of the equation). Eq. (3) results from mass continuity for a fluid with a constant density. While these equations impose local constraints on the transfer of momentum of interacting fluid elements and global constraints on the flow's incompressibility, they provide no insights on the structural evolution of the flow. In particular, the non-linearity of the advective term, $(\mathbf{u} \cdot \nabla) \mathbf{u}$, has made solving these equations mathematically intractable. In fact, determining whether the Navier-Stokes equations remain smooth for all time and do not become singular or "blow-up" remains an

unsolved Millenium Prize problem with a million-dollar reward[15]. With such a limited mathematical understanding of how the solutions to these equations behave, it's no wonder that our physical understanding of turbulence has been hampered for so long.

Given the mathematical challenges of characterizing how turbulent flows develop, researchers began to tackle the problem more abstractly in order to formulate a more fundamental understanding of the interactions that govern the dynamics of turbulent flows. This was initiated by Lewis Fry Richardson in 1922, who poetically encapsulated the interactions of eddies, or whirls, in turbulence:[63]

"Big whirls have little whirls,

That feed on their velocity;

And little whirls have lesser whirls,

And so on to viscosity."

This simple poem was the foundation of the turbulent energy cascade–the mechanism by which the energy of a turbulent flow is transferred from large to small scales. This mechanism, though vague at first, was transformative. It established that large vortices in a turbulent flow interact with each other and break down to smaller vortices, which, themselves, break down in the same manner. This process would iterate again and again until the vortices become so small that their motion is damped out by the viscosity of the fluid. This proposed mechanism for energy transfer seemed intuitive, but it still required a mathematical basis by which the cascade could be characterized and measured in turbulent flows.

Researchers quickly rose to the challenge and began proposing more rigorous mathematical formulations to test the validity of Richardson's energy cascade. While several models were developed and tested, it wasn't until Andrey Kolmogorov's seminal 1941 work that the study of turbulence was forever transformed[34]. Kolmogorov's elegant approach of characterizing turbulent flows was

based on viewing the dynamics of the interacting eddies statistically, abstracting away the details of their structure. Kolmogorov proposed that for turbulent flows at high Reynolds numbers, the small-scale motions of eddies are homogeneous and isotropic. He assumed that as large scale eddies interacted and broke down to smaller scales, they would lose their anisotropic properties, making their dynamics universal and independent of initial or boundary conditions. Kolmogorov then proposed two similarity hypotheses for the dynamics of interacting eddies.

The first similarity assumption states that in every turbulent flow, at a sufficiently high Reynolds number, the dynamics of small-scale eddies are universally and uniquely determined by the eddy size, ℓ, the kinematic viscosity of the fluid, ν, and the rate of energy dissipation per unit mass, ε. From this assumption, Kolmogorov was able to determine a minimum cutoff eddy size, η, at which viscosity dominates and the kinetic energy of the eddy is dissipated as heat:[34]

$$\eta = \left(\frac{\nu^3}{\varepsilon}\right)^{1/4} \tag{4}$$

This established a range of scales over which the turbulent energy cascade is confined. These inertial eddies would have to be larger than the viscous scale but smaller than the large-scale eddies where energy is injected into the flow. Kolmogorov postulated that within this inertial subrange, the dynamics of the interacting eddies are largely unaffected by viscosity. This led to Kolmogorov's second similarity assumption, which states that for turbulent flows at sufficiently high Reynolds numbers, the dynamics of eddies within the inertial subrange are universally and uniquely determined by the eddy size, ℓ, and the energy dissipation rate, ε. Through the use of dimensional analysis, this assumption led to the characterization of the kinetic energy spectrum within the inertial subrange, $E(k)$, known as Kolmogorov's -5/3 law:

$$E(k) = C\varepsilon^{2/3}k^{-5/3} \tag{5}$$

In this scaling law, k, is the mean wavenumber in Fourier space corresponding to an eddy of size, ℓ, such that $k \sim \ell^{-1}$, and C is a constant that is determined experimentally [57]. This scaling law has since become a hallmark of characterizing the statistical behavior of turbulent flows. It has been repeatedly observed in numerical simulations of turbulence as well as experimentally in a multitude of systems, including wind tunnels, atmospheric flows, and the rushing currents of rivers [16]. However, to this day, there is still no unifying theory by which the statistical behavior of Kolmogorov's -5/3 law can be derived from the governing Navier-Stokes equations for turbulent flows.

While Kolmogorov was able to formalize Richardson's vision of an energy cascade by developing a statistical framework for analyzing turbulence, it still has many limitations. This statistical approach is another form of abstraction that obscures the complicated nature of the interacting vortices in turbulence. One of the most notable examples of this is the intermittency of turbulence, which refers to the sporadic and unpredictable "bursts" of the dissipation rate, ε, that are localized both spatially and temporally in turbulent flows [16,24]. The prevalence of these fluctuations, which have been observed numerically and experimentally, arises from the strong, albeit rare interactions of discrete vortices, which deviates from Kolmogorov's similarity assumptions and requires higher-order corrections for the statistical behaviors of turbulent flows [51].

It is natural to attempt to pare down the complexity of such a system through statistics in order to better understand the emergent properties that arise from the interactions of the constituent components. However, broadening our understanding of turbulence also requires the development of a mechanistic framework that characterizes how vortices interact and break down in real space to drive the cascade of energy down to the viscous scale. This bottom-up, mechanistic approach could help to bridge the chasm between the Navier-Stokes equations and Kolmogorov's -5/3 law.

Developing an experimental system to visualize and probe the dynamics of interacting vortices in order to observe and characterize such a mechanism was the motivation that drove the research for this thesis. Many experimental configurations have been developed over the years to character-

ize and quantify the structure of turbulent flows; that is, visualizing the irregular and complicated flow patterns that result from eddies interacting simultaneously over many scales. Experimentally isolating and capturing these dynamics is extremely challenging and often necessitates trade-offs between temporal and spatial resolution. For example, in wall-bounded turbulent flows, like the flow through a pipe, the turbulent eddies are formed along the walls of the channel and are rapidly carried away with the flow. It is thus difficult to track the motion of the eddies as they interact with the rest of the flow while being advected downstream. For examples of stationary turbulence, like the flow that results from an array of jets ejecting fluid at a localized region, the same challenge of localizing the dynamics of the interacting vortices arises. The vortices wrap around one another in a tangled "nest" or "spaghetti-soup" of swirling eddies. The geometries of these vortices undergo rapid transformations as they smash into each other, breaking down into smaller and smaller scales. Even if one could capture the full velocity field of such a stationary flow, which is experimentally very challenging, it is impossible to isolate each eddy from its formation and trace out its lifetime, calculating how the neighboring eddies influence it and lead it to break down. The dynamics are simply too complicated and span too wide of a range of length and time scales.

The work in this thesis centers around a unique, bottom-up approach to understanding how the turbulent cascade evolves in real space, which epitomizes the experimental approach that physicists take in order to understand complicated systems. When particle physicists want to learn how matter behaves on a fundamental level, they take the simplest components of matter, smash them together violently in particle accelerators, and measure what results from the collision. Analogously, we have developed an experimental system to learn about the behavior of the turbulent cascade by smashing together its fundamental components: vortices. Specifically, we have revisited the work of Lim and Nickels[41] by violently colliding two identical vortex rings, head-on into one another in water and visualizing the full 3D dynamics of the resulting breakdown. The symmetry and reproducibility of these collisions have allowed us to precisely localize when and where the colliding vortices break

down. This ability to isolate and track the interactions of the vortices has enabled us to observe by what dynamic, structural mechanisms the vortices interact with each other and break down to form a turbulent cascade.

In Chapter 1, we show experimentally and numerically that for vortex ring collisions at moderate Reynolds numbers, the counter-rotating vortices collide with one another and break down in an iterative manner. When the vortex cores collide, they locally contact and flatten into vortex sheets, which split and roll up into smaller secondary filaments. These secondary filaments, themselves, can also collide with other remaining vortices, and split again in the same manner to form even smaller tertiary filaments. This iterative cascade could be indicative of a possible mechanism by which kinetic energy is conveyed to small scales in turbulent flows. *This chapter was published in Physical Review Fluids as "Cascade leading to the emergence of small structures in vortex ring collisions" in 2018*[45].

In Chapter 2, we demonstrate the existence of a new mechanism in which two counter-rotating vortices violently collide and break down, leading to the rapid development of a turbulent energy cascade mediated by iterations of the elliptical instability. We observe how the onset of the elliptical instability causes the vortex cores to develop antisymmetric perturbations, which give rise to an ordered array of secondary vortex filaments, perpendicular to the original cores. Adjacent pairs of these secondary filaments counter-rotate and interact with each other in the same manner as the original configuration. In the high-Reynolds number limit, we observe another iteration of this instability, whereby a new generation of tertiary filaments forms, perpendicular to the interacting secondary filaments. The energy spectrum of this turbulent breakdown exhibits Kolmogorov's eponymous $k^{-5/3}$ scaling, a hallmark of turbulence. We find that the elliptical instability may play a major role in the formation and sustenance of the turbulent energy cascade. *This chapter was published in Science Advances as "Turbulence generation through an iterative cascade of the elliptical instability" in 2020*[47].

1

Cascade leading to the emergence of small structures in vortex ring collisions

The experiments for this work were developed by Ryan R. McKeown and Shmuel M. Rubinstein and performed by Ryan R. McKeown. The simulations were performed by Rodolfo Ostilla-Mónico and Alain J. Pumir. The data analysis and writing of this work was performed by all of the above authors and Michael P. Brenner. This work has been published in Physical Review Fluids[45].

1.1 Introduction

Our work experimentally and numerically revisits a classical study reported in 1992 by Lim and Nickels, wherein they investigated the instability of vortex filaments during the head-on collision of two dyed vortex rings [41]. They demonstrated that the collision of a red vortex ring with a blue vortex ring gives birth to a tiara of smaller, half-red, half-blue Janus vortex rings, mediated by reconnections of vortex cores. Additionally, Lim and Nickels insightfully remarked that when the the vortex ring collisions are more vigorous, no secondary rings are created; instead, a turbulent cloud forms nearly instantaneously. This turbulent cloud is composed of a multitude of small-scale flow structures, the dynamics of which were too rapid to capture experimentally or numerically at that time.

Vortex tubes can be observed in many flow configurations, from the largest scales [2,65] down to the finest scales in turbulent flows [13,71,25,23]. Their interactions are mediated by many instabilities and may lead to breakdown, reconnection, and annihilation of vortex lines due to viscosity. Vortices can be considered topologically protected, in the sense that without viscosity, a vortex line cannot be broken [31,33,27,44]. Thus, the annihilation of vortex lines is impossible in the infinite Reynolds number limit (or equivalently, in the zero-viscosity limit). At moderate Reynolds numbers, laminar reconnections dominate vortex line interactions [41,56,67,1,49,64,69]. However, at higher Reynolds numbers, interactions become more violent and lose their laminar character [41,40]. The rapid disintegration of coherent vortex structures and formation of small-scale vortices are likely mediated by a combination of various well-studied vortex instabilities [10,78,3,81,29,35,39]. Nevertheless, many questions remain regarding the dynamics that initiate the breakdown of vortices from large to small scales.

In this work, we examine the conceptually simple configuration of two identical vortex rings colliding head-on [55]. The early experimental results of [41] indicate—for collisions at sufficiently high

Reynolds numbers—the development of a violent interaction between the rings, causing them to rapidly disintegrate into a turbulent cloud. Due to the very small temporal and spatial scales involved in this interaction process, it has not been possible to study in detail the interaction that initiates the complete breakdown of the vortices. By using state-of-the art visualization techniques, we investigate with sufficient temporal and spatial resolution how this violent interaction breaks down the colliding vortex rings.

From a fundamental point of view, understanding the formation of small-scale flow structures over very short times is a classical problem in fluid mechanics[77], as it is expected to play an important role not only in vortex reconnection, but more generally in turbulent flows[16]. It has been recognized that the close-range interaction of vortices is also a prime candidate for the formation of singularities in the inviscid 3D fluid equations, although the numerical evidence for or against the existence of such solutions has been ambiguous[9,5,60,26,22].

Recently, a new class of mechanisms for energy transfer has been proposed, in which the kinetic energy of a flow is conveyed from large to small scales via an iterative cascade, with the same elementary process repeating again and again on smaller and smaller scales[6,74], reminiscent of early simulations[58,60,26,28]. Analogous iterative instabilities have been previously observed in the breaking of fluid jets into droplets[7,70]. The physical realization of this iterative process leading to the emergence of small flow structures is envisioned through the interaction between two antiparallel vortex filaments[72,59], whose collision is described by a universal similarity solution[6]. The filaments become perturbed and develop into a characteristic shape reminiscent of two opposing tents. The collision initiates at the nose of the tents, leading to what will be referred throughout the text as tent-like structures[6]. As a result of the collision, the filaments flatten into extremely thin vortex sheets. An iterative cascade of instabilities occurs if the sheets, themselves, break up into smaller vortex filaments which subsequently collide, flattening and breaking down into even thinner filaments. Estimates show that these dynamics occur over fleeting time-scales and diminutive length scales[6]. To date, it

has not been possible to directly observe the extreme flattening of colliding vortex cores, followed by their subsequent breakdown into secondary and tertiary filaments, as documented here.

1.2 Methods and Materials

Directly observing the breakdown of large coherent vortices into a turbulent cloud requires the visualization of large flow structures disintegrating over ephemeral time-scales (a few milliseconds) into the smallest constituents of turbulent flow (micrometer length scales). The difficulty results from the chaotic spatiotemporal nature of these processes, making them hard to pin down. In order to isolate and experimentally probe the emergence of the turbulent cloud that results from the breakdown of colliding vortices, we examine the head-on collision of two identical vortex rings, as shown in Fig. 1.1(a) and video 1 [41,46]. The planar geometry of the vortex ring collision restricts all of the dynamics to occur within a narrow volume whose position is fixed in the laboratory frame. This confinement allows for the real-time, high speed, and fully three-dimensional visualization of the flow. Our experimental setup is shown in Fig. 1.1(b-c) and described in detail in Appendix A.1.

Two vortex rings are fired head-on using a piston-cylinder assembly in a 75-gallon water aquarium ($45 \times 122 \times 50$ cm^3). The vortex cannons are capable of reaching a maximum Reynolds number, Re $= UD/\nu$, of 25,000 and a maximum stroke ratio, SR $= L/D$, of 4 [18]. U and L are the piston velocity and stroke length, respectively, ν is the kinematic viscosity of the fluid, and $D = 2.54$ cm is the tube diameter. The cores of the vortex rings, where the vorticity of the flow is concentrated, are dyed[67] with a fluorescent dye (Rhodamine B) in order to track their motion and deformation. Complementary two-dimensional particle-image velocimetry (PIV) measurements were conducted to ensure that the injected dye coincides with the vortex cores during the collision, as discussed further in Appendix A.2. The breakdown dynamics of the cores are directly visualized in real time and in full 3D. The collision plane is illuminated by a pulsed ($\approx$ 15 ns), 2-Watt laser sheet (Spect-
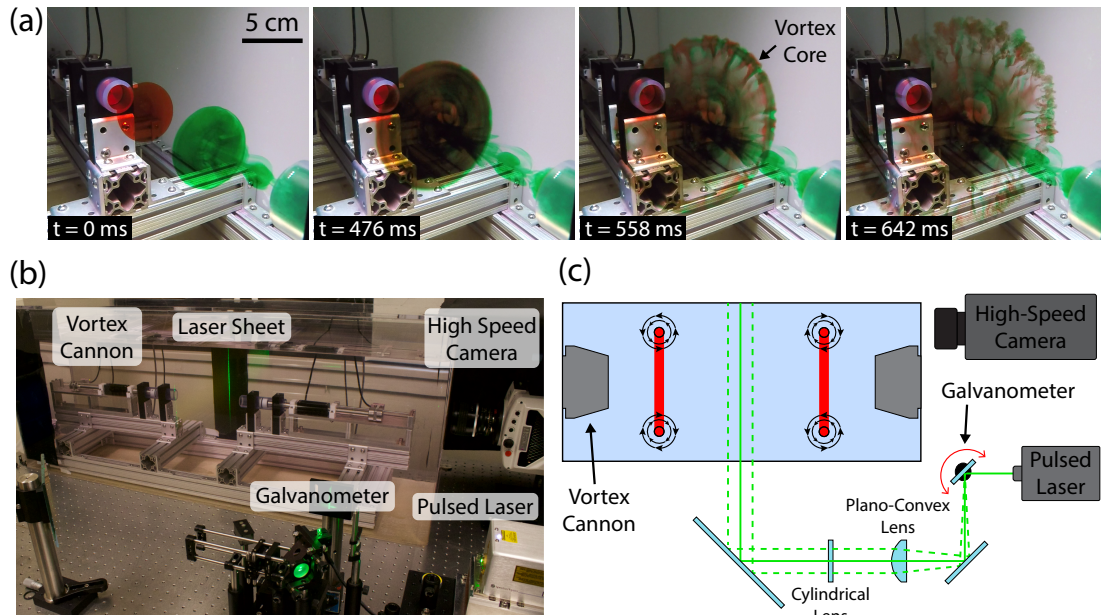
Figure 1.1: Experimental system. (a) A montage of images showing the head-on collision of two vortex rings formed at Re = 8000 and SR = 2.5, where both rings are dyed with food coloring. Upon first colliding, the vortex rings stretch and grow radially before rapidly breaking down to fine-scale "smoke." (b) An image and (c) schematic of the two vortex cannons and high-speed scanning laser sheet fluorescence microscopy setup, which enables each scan of the flow to be reconstructed into a 3D volume.

raphysics Explorer One 532-2W), synchronized with the exposure signal of a high-speed imaging sensor (Phantom V2511). The laser sheet scans through the flow over a distance of up to 2.54 cm at a frequency of 1 kHz, allowing a data capture rate of 1,000 volumes per second; this high scanning rate ensures that the dynamics of the flow are effectively "frozen" in each individual scan. The full 3D spatiotemporal dynamics of the vortex cores are reconstructed with Dragonfly visualization software (Object Research Systems) at a maximal spatial resolution of 145 μm along the collision plane and 100 μm in the scanning direction.
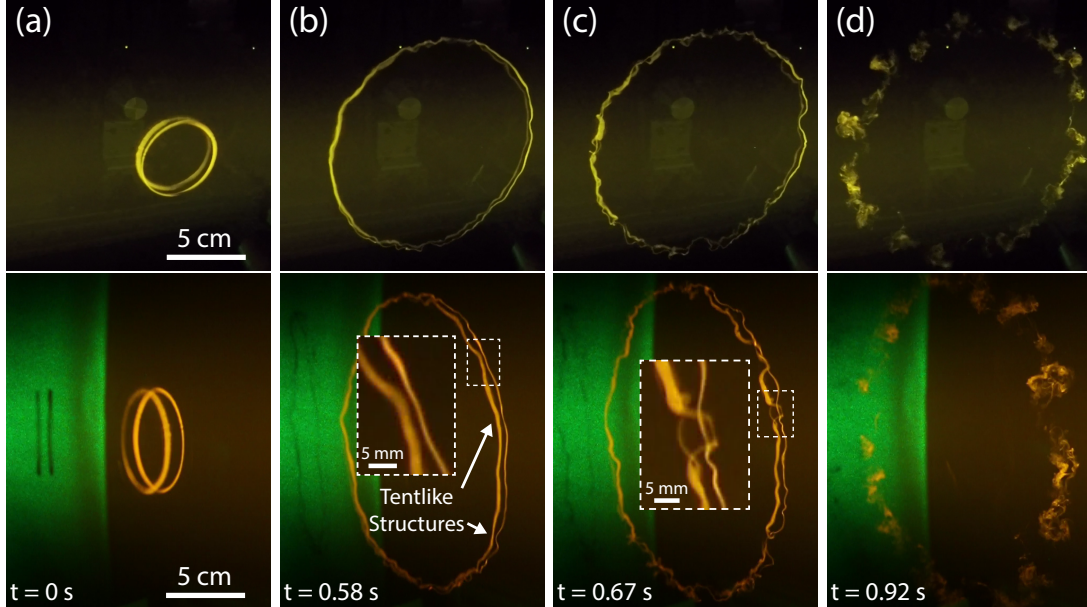
Figure 1.2: Two vortex rings colliding. Four consecutive snapshots simultaneously taken from the front (top) and side (bottom) showing the progressive stages of the head-on collision between two identical vortex rings with Re = 4000 and SR = 2.5. Both cores are injected with a small volume of fluorescent dye (Rhodamine B) and illuminated from the side by a scanning green laser sheet, highlighting the core in bright yellow. (a) As the two cores approach, they stretch radially but remain circular. (b) With further stretching, the vortex rings develop long-wavelength perturbations that form tent-like structures. (Inset) Zoomed-in view of a developing tent-like structure. (c) The tips of the tent-like structures flatten due to the intense strains exerted by the circulating cores. (Inset) The flattened core stretches into a vortex sheet and splits into two secondary vortex filaments. (d) The initial breakdown of the vortex cores at these local tent-like structures propagate along the vortex cores, leading to the annihilation of the vortex rings and the formation of a turbulent cloud.

1.3 Vortex Ring Collisions

The collision between two vortex rings occurs over several distinct stages, shown for a typical example in Fig. 1.2 and video 2[46]. As the two rings initially approach one another, they expand radially, stretching along the collision plane, as shown in Fig. 1.2(a). This stretching is initially uniform, such that the rings maintain a toroidal shape. Eventually, however, azimuthal undulations develop circumferentially into unstable tent-like structures around the vortex rings, as shown in Fig. 1.2(b-c). The undulations grow, contact, and initiate the complete breakdown of the coherent cores into a

tiara of turbulent puffs, shown in Fig. 1.2(d).

The observed initial azimuthal undulations of the core can arise from two different mechanisms[39]: the Crow instability[10] and the elliptical instability[53,78]. The Crow instability develops from the interaction of the two vortex rings and has a wavelength on the order of the distance between the rings, much larger than the core radius, σ. In contrast, the elliptical instability occurs from a resonant interaction of a single vortex ring with a strain field, either from itself or from the other vortex, and has a wavelength on the order of the core size. The current experiment has an initial instability that is consistent with the Crow instability, which leads to the initial formation of tent-like structures. As the Reynolds number increases, we expect that the ensuing dynamics will become richer and more complicated as a result of the interplay between the different types of instabilities[39].
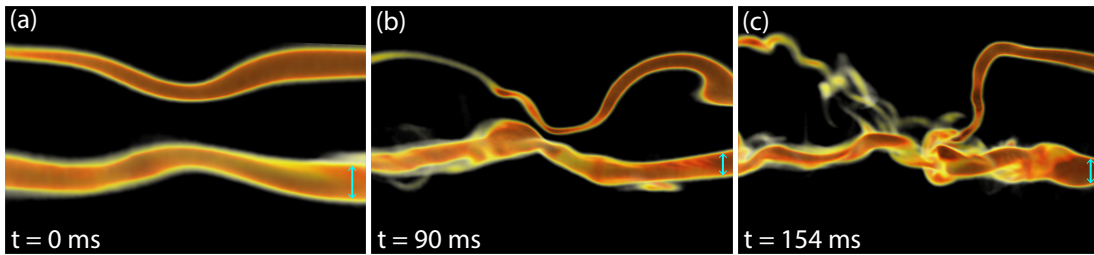
Figure 1.3: 3D reconstruction of the breakdown of two dyed vortex cores. Three snapshots showing the late-stage dynamics of two colliding vortex rings where Re = 4000 and SR = 2.5. (a) The cores deflect toward one another, developing a tent-like structure. (b) The tent-like structure grows in amplitude, and the lower core flattens into a vortex sheet at the region where the two cores are closest. (c) The cores contact and break down. In all panels, the cyan arrows indicate length scales: (a) 1.7 mm, (b) 1.4 mm, and (c) 1.4 mm.

The nonlinear dynamics—following the initial formation of the long-wavelength undulations—develop the two vortex cores into opposing tent-like structures, as shown by the 3D reconstruction of a typical collision of two dyed filaments in Fig. 1.3(a-c) and in video 3[46]. The tent-like structures grow as a result of the mutual strain imposed by the two interacting vortex cores. At the point of shortest separation, the strain is the strongest, which amplifies the local curvature of the filaments. Eventually, the mutual strain becomes so strong that the lower core flattens into a vortex sheet, as

15

shown in Fig. 1.3(b). This vortex sheet flattens to a thickness that is approximately one tenth that of the initial core diameter, consistent with theoretical predictions[6]. Ultimately, the vortex sheet breaks down completely, as shown in Fig. 1.3(c).

1.4 Vortex Core Breakdown

Imaging the dynamics beyond the formation of tent-like structures requires increased spatial and temporal resolution. The dynamics of both vortex cores are rapid and three-dimensional, making them difficult to distinguish clearly when both cores are dyed. However, they are clearly discernible when only one cores is injected with dye while the other remains invisible, as shown for a typical example in Figs. 1.4-1.5.

The initial breakdown of the dyed vortex core can be characterized by slicing through the 3D reconstruction and examining the deformation of the core's cross section, as shown in Fig. 1.4(a). The vortex core stretches and deforms into a curved vortex sheet as a result of the strain exerted upon it by the counter-rotating undyed core, as shown in Fig. 1.4(a). The centerline length of the vortex core grows linearly to nearly four times its initial length, as shown in Fig. 1.4(b). While the stretching of the dyed core is initially uniform, when the end-to-end distance of the core reaches three times its initial length, the ends of the core bulge as the dye and likely the vorticity are continuously drawn from the center of the sheet to the edges. Concomitantly, the center of the vortex sheet contracts and thins until its thickness reaches our spatial resolution limit, as shown in Fig. 1.4(c). As a result of this intense stretching and thinning of the vortex sheet, the aspect ratio of the core approaches a value of 100:1 before the dye in the center of the vortex sheet becomes too dilute to resolve and the bulges at the edges of the sheet roll up into secondary vortex filaments.
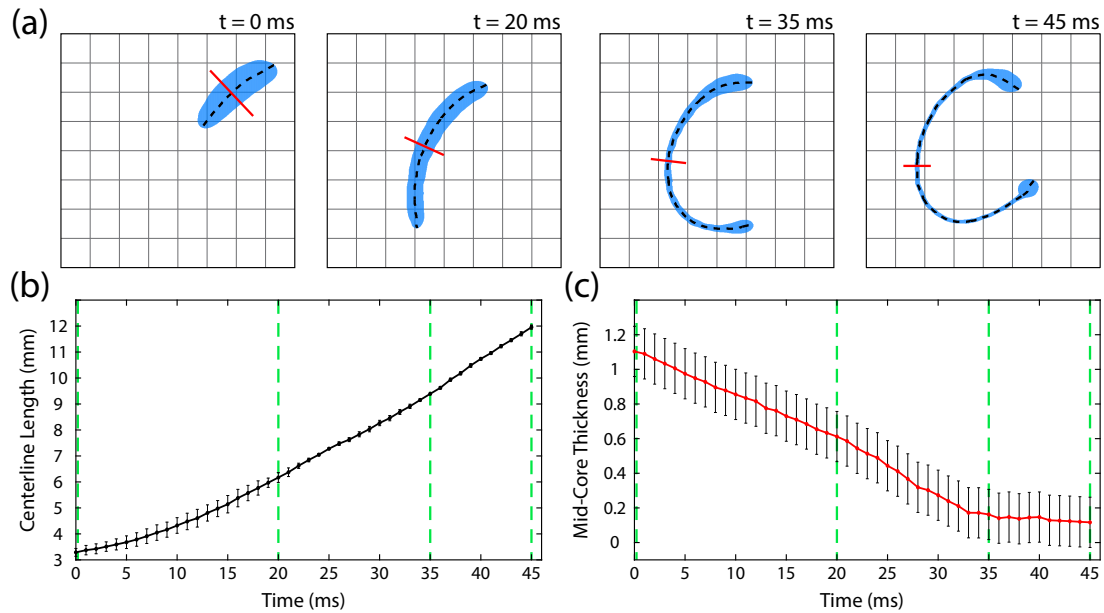
Figure 1.4: Extreme stretching of a colliding vortex core. (a) Cross-sectional slice of a deforming vortex core extracted from 3D flow visualization during the collision of a dyed vortex ring with an invisible, undyed vortex ring. The dyed vortex core, rotating in the clockwise direction, is shown in blue and is stretched by the undyed vortex core, which rotates in the counter-clockwise direction. The centerline of the vortex core is indicated by the black dashed line, and the plane perpendicular to the midpoint of the centerline is shown by the red lines. The grid spacing is 1 mm $\times$ 1 mm. (b) Centerline length vs. time for the dyed core. (c) Core thickness along the midpoint of the centerline vs. time. The green dashed lines correspond to the times indicated in (a), the data in both plots is averaged over 10 adjoining slices, and for this collision, Re = 4000 and SR = 2.5.

During the later stages of the breakdown, however, the colliding vortex cores undergo far more complicated three-dimensional dynamics, as shown in Fig. 1.5 and videos 4-5 [46]. Initially, the dyed vortex is distorted by the interaction with the partner vortex and forms a tent-like structure, as shown at $t = 0$ ms in Fig. 1.5(a). This interaction causes the vortex to flatten into an extremely thin vortex sheet, as shown in Fig. 1.5(b). The vortex sheet continues to thin, and the dye gradually collects at the edges, as shown in Fig. 1.5(c). Eventually, the intensity of the vorticity in the center the sheet becomes very small, and concentrates into two new filaments emerging from the edges of the sheet, as shown in Fig. 1.5(d). The secondary filaments undergo complicated three-dimensional motion as they unravel the original vortex core. Eventually, the daughter filaments, themselves, split into even thinner tertiary filaments, as indicated in Fig. 1.5(e-f). The tertiary filaments are so thin, that they are difficult to resolve, but enhancing the contrast reveals a complex topology of fine, multi-scale filaments, as shown in the inset of Fig. 1.5(f). The tertiary filaments continue to stretch and interact with each other, the secondary filaments, and with the undyed vortex, as shown in Fig. 1.5(g-h).

The essence of the overall breakdown mechanism is captured elegantly in a single moment which simultaneously showcases three generations of vortices in the iterative cascade, as shown in Fig. 1.5(i)— the primary vortex core splits into secondary filaments, which then split again into tertiary filaments. The fluorescent dye that is injected into the vortex cores effectively traces their position and slightly under-estimates their size, defined by the vorticity distribution in the cores detailed in Appendix A.2. The mean thickness of the initial primary, secondary, and tertiary cores is approximately 1.83 ± 0.1 mm, 0.61 ± 0.1 mm, and 0.22 ± 0.1 mm, respectively. The same intensity threshold is maintained during the measurement of each core size, and the topology of the filaments is quite stable over a wide range of intensity thresholds. Thus, at each iteration of the breakdown, the vortex core size decreases by a factor of three. As the iterative breakdown process generates smaller and smaller scales of vortices, it is ultimately halted by viscosity. This therefore suggests that the itera-

Figure 1.5 *(following page):* An iterative cascade of instabilities leads to the emergence of small-scale flow structures. 3D reconstruction of the breakdown dynamics following the collision of a dyed vortex ring (top) with an invisible undyed one (bottom). For this typical example, Re = 4000 and SR = 2.5. (a) The upper dyed vortex develops a tent-like perturbation that deflects toward the undyed lower vortex. (b) The tent-like structure flattens into a very thin vortex sheet. Most of the dye collects at the edges of the sheet. (c) The thin vortex sheet ruptures, and a hole is formed, which extends down the rest of the core. (d) The vortex sheet splits into two smaller secondary filaments, which unravel the vortex core at both ends. (e) A secondary vortex splits into smaller tertiary vortex filaments. (f) A complex structure of interacting secondary and tertiary vortex filaments emerges. (Inset) Zoomed-in and contrast-enhanced view showing a network of interacting coherent secondary and tertiary vortex filaments. The magnified view is a sub-volume of the main panel indicated by the dashed box and is viewed through the dashed magenta window. (g-h) Full view of the emerging tertiary filaments. The contrast is enhanced to highlight the faint tertiary filaments. (i) The essence of the dynamics is captured entirely in one snapshot, simultaneously showing three generations of the iterative cascade. In every panel, the size of a distinct feature is indicated by a cyan scale bar: (a) 1.3 mm, (b) 1.2 mm, (c) 1.2 mm, (d) 1.7 mm, (e) 2.9 mm, (f) 2.1 mm, (Inset) 1.1 mm, (g) 1.1 mm, (h) 0.6 mm, and (i) 2.8 mm.

Figure 1.5: (continued)

(a) Dyed Vortex
Undyed Vortex (invisible)
t = 0 ms

(b) Vortex Sheet
t = 16 ms

(c) t = 22 ms

(d) Secondary Filaments
t = 40 ms

(e) Tertiary Filaments
t = 63 ms

(f) t = 79 ms
Tertiary Filaments

(g) Tertiary Filaments
t = 79 ms

(h) Tertiary Filaments
t = 88 ms

(i) Vortex Core → Secondary Filaments → Tertiary Filaments
t = 67 ms
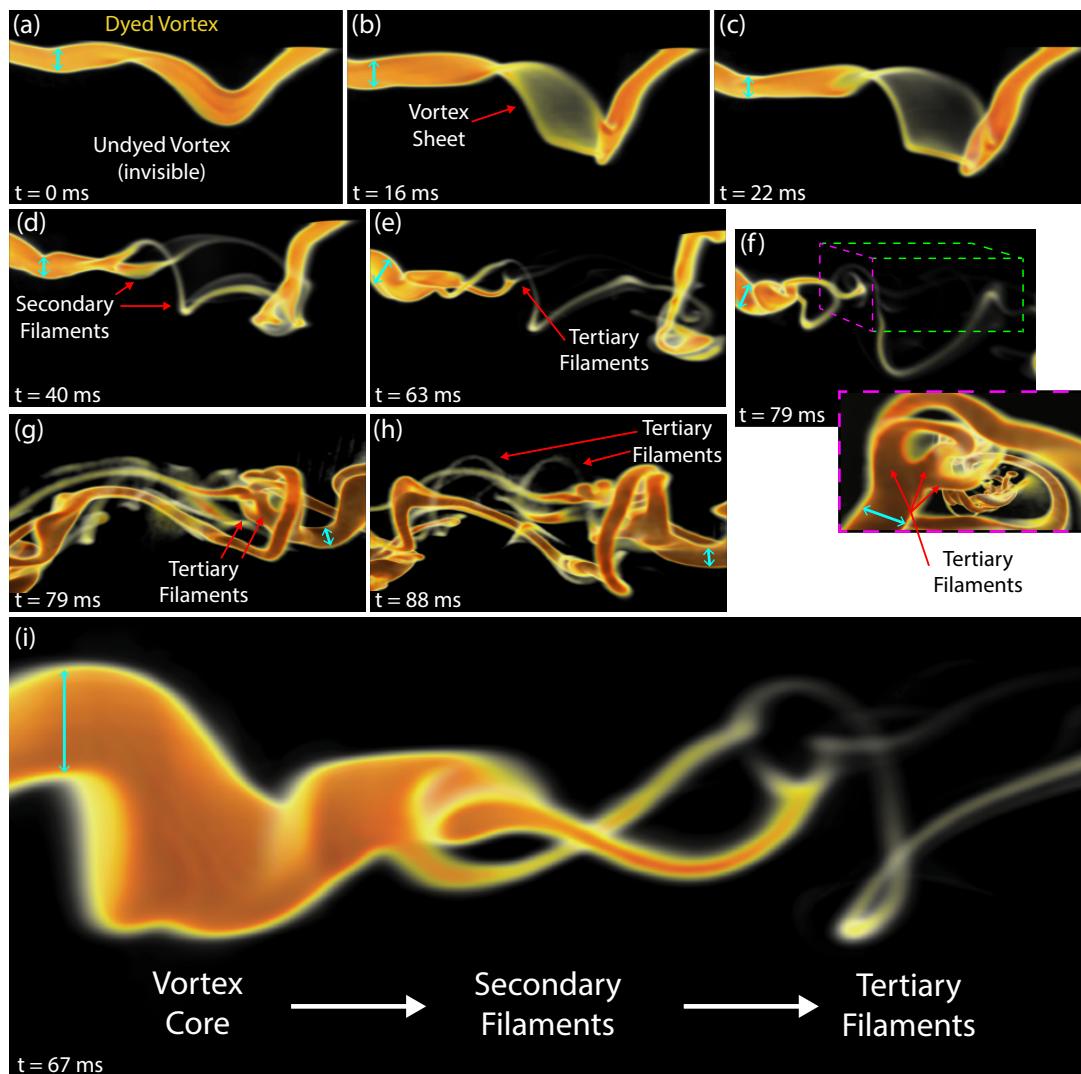
tive cascade could continue and repeat itself to even smaller scales during higher Reynolds number collisions.

Nevertheless, it is important to point out that viscous effects play a critical role even in the breakdown of the primary vortex core. Viscous effects are required for the topological change in which the vortex sheet splits into secondary filaments, clearly shown in Fig. 1.5(b-c). Viscosity acts only for short times and on small scales when the sheet is stretched thinly and appears to rupture. Additionally, it is important to stress that three-dimensional effects play an essential role in the breakdown dynamics. While the splitting of the vortex sheet into smaller filaments may seem to be a quasi-two-dimensional phenomenon, the relative motion of the vortex filaments is induced both from individual vortex filaments, from interactions with neighboring filaments, and vortex stretching.

1.5 Direct Numerical Simulations

To probe this breakdown mechanism further, we also examine the head-on collision of two vortex rings with direct numerical simulations of the Navier-Stokes equations. Technical details of the simulations are described in Appendix A.3. In the same configuration as the experiments, the initial condition for the simulations consists of two identical vortex rings colliding head-on. In the calculation shown here, the Reynolds number, defined by $\mathrm{Re}_\Gamma = \Gamma/\nu$, where Γ is the circulation of the rings, is $\mathrm{Re}_\Gamma = 3500$. The initial core slenderness ratio, $\Lambda = \sigma/R$, is set at 0.35, where R is the vortex ring radius. Throughout the progression of the simulation, we calculate both the evolution of the vorticity distribution as well as the concentration of an advected dye in both vortex rings. Computational limitations prohibit using a dye diffusivity comparable to that of the experiments, $\approx 10^{-3}\,\nu$[17]. The simulated dye diffusivity is equal to the kinematic viscosity of the fluid. The initial dynamics mirror those of the experiments, as shown in Fig. 1.6(a)—the rings expand radially as they approach one another and develop a long-wavelength Crow instability[39].
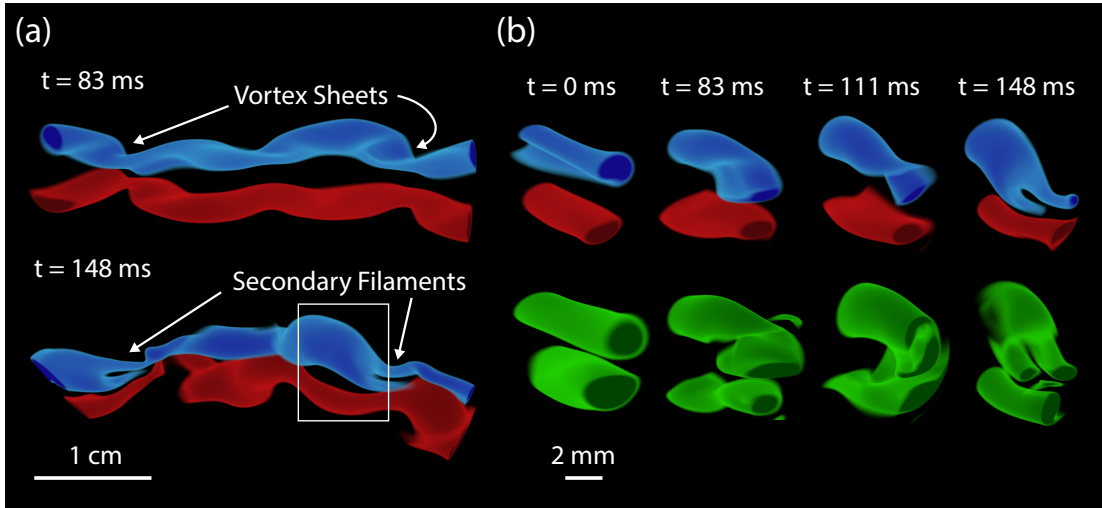
Figure 1.6: Numerical simulation of colliding vortex rings. (a) Volumetric plot of dye concentration in a simulation of two colliding vortex rings whose cores are initially seeded with red and blue dye, respectively. As the vortex cores approach, the blue vortex flattens into thin vortex sheets, which break down into secondary filaments. (b) Zoomed-in, cross-sectional view of the developing secondary filaments indicated by the white box in (a). The top panels plot the dye concentration, and the bottom panels plot the vorticity modulus. The formation and rupture of sheets into filaments is clearly shown by the top (blue) vortex, while the lower vortex shows that if no rupture occurs, the sheet eventually curls back into a vortex when the strain is released.

The simulations nicely capture one iteration of the cascade mechanism, as shown in Fig. 1.6(b) and video 6[46]. The dye tracks the vorticity during the initial development of the instability and formation of the tent-like structures. The dynamics of the simulations are qualitatively similar to those of the experiments as one of the dyed vortex cores flattens into a sheet, which then ruptures into two secondary filaments. These same dynamics are mirrored in the vorticity distribution, as shown in green in Fig. 1.6(b). The circulation is distributed between the two ruptured filaments in a 2:1 proportion, and its sum roughly corresponds to the pre-split sheet configuration, with minor losses ($< 1\%$), likely due to viscosity. The diffusive losses for the dye are larger: $\approx 40\%$ (a similar phenomena is also seen by the evanescent secondary filaments in Fig. 1.5(i)), but the ratio between the amount of dye in both secondary filaments matches those of the circulations. The simulations suggest that the minimum thickness of the sheet joining the two secondary filaments is given by

the viscosity of the fluid. If $\dot{\gamma}$ is the shear rate through which the sheet is being stretched, viscous effects will set in when the sheet thickness is of order $\sqrt{\nu/\dot{\gamma}}$. This viscous length scale is calculated to be approximately 0.005R for the vortex sheet at $t = 111$ ms, the same order as the thickness of the sheet ($\approx 0.01R$). This is approximately 4 grid points. While the rupture of the sheet is not produced in a strict sense—i.e. no region with zero vorticity appears—at later times, the vorticity in the sheet remnants becomes vanishingly small and the flow structure can be effectively thought of as two discrete secondary filaments. Vorticity amplification is primarily localized to the breakdown of the vortex cores, while the mean vorticity of the simulation is amplified only slightly. Additionally, the whole collision process tends to make the vorticity lose its initially preferential orientation in the azimuthal direction, indicating the emergence of a turbulent cloud like in the experiments. In Appendix A.4, we show more details about the evolution of vorticity in the simulations.

1.6 CONCLUSION

Vortex ring collisions at high Reynolds numbers lead to a near-instantaneous breakdown of the initial vortices into a turbulent cloud. We have shown that the formation of this cloud is initiated by an iterative cascade of instabilities: colliding vortex filaments break down into smaller secondary filaments, which then interact with each other and break down into even smaller tertiary filaments. To our knowledge, this is the first reported experimental observation of a dynamic cascade of instabilities in a bulk fluid. The iterative mechanism, whereby large vortex filaments flatten into sheets and then break down into smaller filaments, qualitatively agrees with recent theoretical predictions[6,74], although the mechanism observed experimentally and numerically differs in details from the one envisioned in[6]. The degree to which the vortices stretch during each step of the cascade is a crucial question to understand the possible relevance of the scenario discovered here to the singularity problem in the inviscid equations of fluid motion[9,15,50]. A semi-quantitative modelling approach

23

may provide much-needed insight. Viscosity must play an essential, though limited, role at each iteration, as it enables the topological transition that leads to the rupture of the vortex sheets. The observation that vortex ring collisions lead to such complicated dynamics on ever smaller length scales, with viscosity playing such a critical role, therefore exposes the subtlety of understanding the singular or near-singular dynamics of the Euler and Navier-Stokes equations.

Because the breakdown dynamics that emerge in the head-on collision of vortex rings occur locally through the close-range interactions of vortex filaments, one may speculate that it could be extended to other high-Reynolds number flows. In fact, this mechanism could conceivably supply an effective means for a flow to rapidly convey energy down to the smallest constitutive scales, indicative of the type of dynamics that could lead to the turbulent cascade itself—reminiscent of, but perhaps different from Richardson's initial proposal[63]. While the mechanism uncovered here may be involved in the proliferation of small-scale vortex structures in turbulent flows—documented many times both experimentally[13] and numerically[71,25,23]—our measurements occur at comparatively moderate Reynolds numbers. We expect that richer breakdown dynamics have yet to be observed for collisions at higher Reynolds numbers. Nevertheless, our model system provides an exciting new lens through which we can attempt to observe and characterize the emergence of complex, multi-scale flows in real-time. By identifying the mechanisms by which these vortical flows break down to small scales, we hope to develop a new framework for viewing the turbulent cascade as a collection of discrete dynamic instabilities. Our study therefore indicates that the rigorous investigation of colliding vortex rings, at high spatial and temporal resolution, may potentially provide profound insights on both the fundamental physics of vortex breakdown and the deep underlying mathematical foundations that govern the emergence of small scales in violent turbulent flows.

2

Turbulence generation through an iterative cascade of the elliptical instability

2.1 Introduction

Understanding how turbulent flows develop and organize has puzzled scientists and engineers for centuries[36]. The foundational characterization of turbulent flow began with Reynolds over a century ago[62] and was quickly followed by rigorous statistical interpretations of how turbulent flows develop[75,63,14]. In 1937, Taylor and Green[76] introduced an initial flow condition which produces a cascade of energy from large to small scales. Subsequently, Kolmogorov postulated that turbulent flows exhibit universal behaviors over many length scales. Kolmogorov[34] predicted that within an inertial subrange, the energy spectrum of a turbulent flow has a universal, self-similar form wherein the energy scales as the inverse 5/3 power of the wavenumber k. Kolmogorov's energy cascade has been observed in a plethora of experimental systems and numerical simulations, from wind tunnels to river beds, see e.g. Fig.13 of Chapman[8].

The efficient conveyance of energy from the large scales, where it is injected, to the small scales, where it is dissipated, is at the heart of how complex, three dimensional flows are maintained. It is thus critical to understand how small-scale flow structures are formed and maintained at high Reynolds numbers. In spite of major progress in providing an effective statistical description of turbulent flows[57], our understanding of the mechanisms by which interactions between eddies are mediated remains limited. In fact, the explanations of how this occurs in real-space are often abstract and "poetic"[63,4,30].

The temporal development of the turbulent cascade remains one of the most intriguing mysteries in fluid mechanics. In particular, it is not well understood what specific mechanisms lead to the development of large velocity gradients in turbulent flows. These large velocity gradients, which derive from the interactions of turbulent eddies, amplify the kinetic energy dissipation rate, ε, in a manner that is independent of the fluid viscosity in the high-Reynolds number limit[14,16]. This implies the existence of an inertial mechanism by which vortices locally interact to convey energy across scales

such that the statistical properties of the energy cascade develop in accordance with the scaling laws established by Kolmogorov. Note that the limit to how fast an initially regular flow may produce extremely large velocity gradients is also a celebrated mathematical problem[15]. It is therefore of great interest to look directly for elementary flow configurations of interacting vortices that begin smooth and rapidly develop into turbulence. This approach was implemented by Lundgren[43], who analytically examined the breakdown of a single vortex under axial strain, bursting into an ensemble of helical vortex bundles. While this configuration has been observed to lead to the development of a turbulent flow, it requires the presence of a particular, large-scale strain configuration acting on an isolated vortex[11]. We implement a more general flow configuration that typifies the fundamental components of the turbulent cascade: the collision of two identical vortices. Recent numerical and experimental works demonstrate that the breakdown of colliding vortex rings at intermediate Reynolds numbers gives rise to small-scale flow structures[45], mediated by the iterative flattening and splitting of the vortex cores to smaller and smaller filaments[6,59].

Here, we revisit the emergence of a turbulent burst of fine-scale flow structures that results from the violent, head-on collision of two coherent vortex rings[41,45]. This classical configuration is a unique model system for probing the development of turbulence without any rigid boundaries or large-scale constraints. We show that for high Reynolds numbers, the violent breakdown of the colliding vortex rings into a turbulent "soup" of interacting vortices is mediated by the elliptical instability. During the late-stage, nonlinear development of the elliptical instability, an ordered array of antiparallel secondary vortex filaments emerges perpendicular to the collision plane. Locally, these pairs of counter-rotating secondary filaments spawn another generation of tertiary vortex filaments, resulting in the expeditious formation of a hierarchy of vortices over many scales. Our numerical simulations show that at this stage of the breakdown, the interacting tangle of vortices reaches a turbulent state, such that the energy spectrum of the flow exhibits Kolmogorov scaling. We observe both experimentally and numerically how the elliptical instability precipitates the onset

of turbulence, generating and maintaining the means by which the energy of the flow cascades from large to small scales.

2.2 Vortex ring collisions

The geometry of the experimental setup is depicted schematically in Fig. 2.1(A). Two identical counter-rotating vortex rings are fired head-on in a 75-gallon aquarium filled with deionized water, as shown in Movie S1[48]. The vortex rings are formed via a piston-cylinder configuration in which a slug fluid with viscosity, ν, is pushed through a cylinder of diameter, D (2.54 cm), at a constant velocity, U, with a stroke, L. The resulting flow is controlled by two dimensionless parameters: the Reynolds number, Re = UD/ν, and the stroke ratio, SR = L/D[18]. Fluorescent dye (Rhodamine B) is injected into the cores of the rings as they are formed. Since the collision occurs at a fixed plane in the laboratory frame, this configuration is attractive for directly observing the rapid formation of small-scale flow structures. The dynamics and eventual breakdown of the dyed cores are visualized in full 3D by imaging over the collision plane with a scanning laser sheet ($\lambda = 532$ nm), which is pulsed synchronously with a high-speed camera (Phantom V2511). The technical details of how the vortex rings are formed and visualized in 3D are described in previous work[45] and in Appendix B.1. Additionally, we perform direct numerical simulations (DNS) of interacting vortices at Reynolds numbers equivalent to the experiments (see Appendix B.1- B.2 for how the definitions of the Reynolds numbers in simulations and experiments compare).

As the vortex rings collide, they exert mutual strains on one another, causing them to stretch radially at a constant velocity before breaking down at a terminal radius, as shown in Fig. 2.1(B). At low Reynolds numbers, Re $\lesssim$ 5000, the dyed cores break down, ejecting a tiara of secondary vortex rings or smoky turbulent puffs[41,45] at approximately 6 times the initial radius, R_0. The initial vortex ring radius and core radius, σ, were measured separately through particle image velocime-
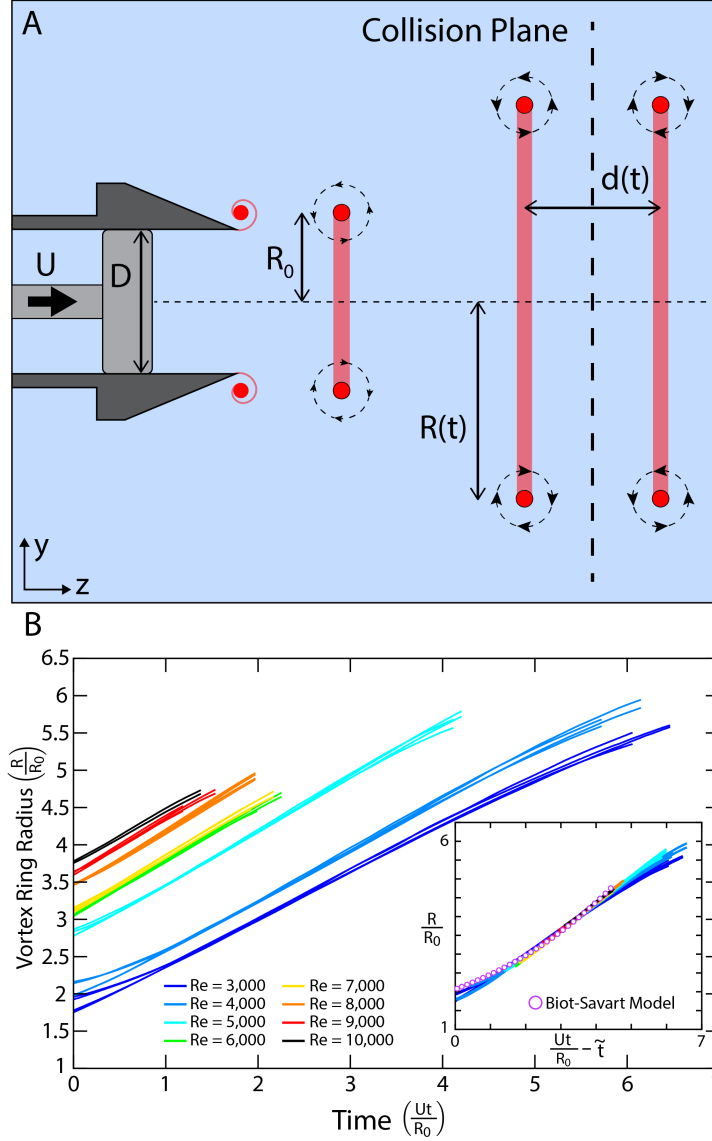
Figure 2.1: Vortex ring collisions. (A) Schematic side-view showing the formation and collision of dyed vortex rings in experiments. Fluorescent dye (Rhodamine B) is injected into the core of the vortex via a thin gap in the orifice of the vortex cannon. The dashed horizontal line denotes the symmetry axis. (B) Vortex ring radius vs. rescaled time for collisions at various Reynolds numbers. Both cores are dyed, the core centerlines are extracted from 3D reconstructions, and the centerlines are fitted to circles with a fixed center point. The initial time begins when the vortex rings enter the scanning volume and ends when the vortex cores break down. (inset) All experimental curves shifted by $\tilde{t}$ to collapse. The radial growth of the rings coincides with the Biot-Savart prediction.

try (PIV), as described in Appendix B.2. Strikingly, for collisions at higher Reynolds numbers, Re $\gtrsim 5000$, the cores "burst" into an amorphous turbulent cloud of dye at a maximum radius of approximately $5R_0$, indicating the onset of a different breakdown mechanism at this high Reynolds number regime. The mean radial growth of the colliding rings is well described by the Biot-Savart model[2], as described in Appendix B.3.1- B.3.2. Additionally, the radial expansion of the rings is encapsulated by a universal functional form, as shown in the inset of Fig. 2.1(B).

2.3   Onset of the elliptical instability: Vortex core perturbations

While the mean radial growth of the colliding vortex rings follows the same linear evolution at any Reynolds number, the cores themselves develop different forms of perturbations, due to their mutual interaction. The formation of these perturbations can arise from two different types of instabilities. The Crow instability[10] causes the cores to develop symmetric circumferential perturbations with long wavelengths, much larger than the core radius, σ. This instability stems from the mutual advection of the interacting vortices[39] and governs the breakdown dynamics for collisions at lower Reynolds numbers[41,45,39]. The nonlinear development of the Crow instability causes the rings to deflect into one another and form "tent-like" structures[21,6,45], which interact locally at the collision plane.

At higher Reynolds numbers, both our experiments and simulations show that the breakdown dynamics are governed by the elliptical instability, causing the vortex cores to develop short-wavelength perturbations on the order of the core radius[78,53,66] (see Appendix B.3.3). This instability originates from the parametric excitation of Kelvin modes in the vortex cores due to the resonant interaction of the strain field from the other vortex[39,29]. A hallmark of the elliptical instability, these short-wavelength perturbations grow synchronously in an antisymmetric manner, as shown for two typical experimental and numerical examples in Fig. 2.2(A-B).
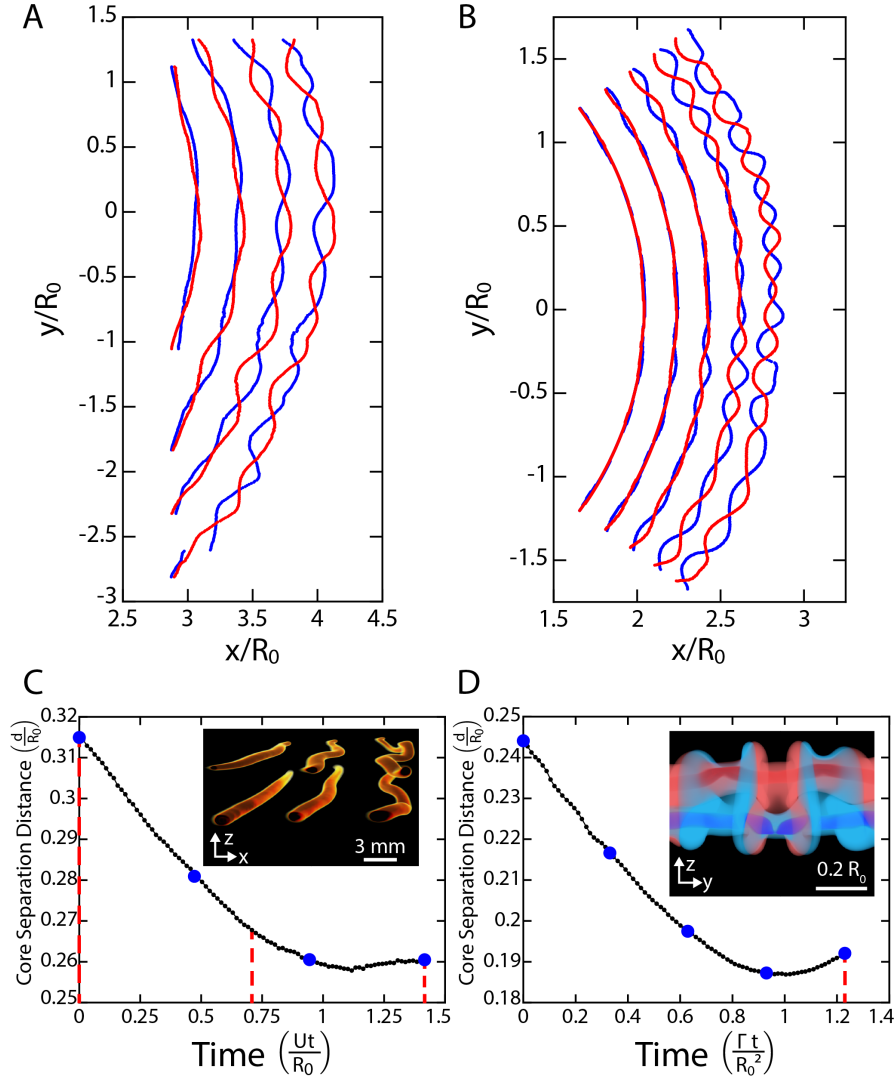
Figure 2.2: Antisymmetric perturbations in vortex ring collisions. A montage of core centerline trajectories for vortex ring collisions in both (A) experiment and (B) direct numerical simulation. The top ($z > 0$) cores are indicated by the red lines, and the bottom ($z < 0$) cores are indicated by the blue lines. For the experimental collision, Re = 7000, SR = 2, and R_0 = 17.5 mm. For the DNS collision, $Re_\Gamma = \Gamma/\nu$ = 4500 and $\sigma = 0.1R_0$. The cores are segmented from the 3D flow visualization in the experimental collision and from the pressure distribution in the simulation. Mean core separation distance vs. rescaled time for the same (C) experimental and (D) numerical collisions. The blue circles correspond to the trajectories in (A) and (B), and the red dashed lines correspond to the visualizations in the insets. (C, inset) 3D visualization of the dyed vortex cores in the experimental collision. (D, inset) 3D visualization of the dyed vortex rings in the simulation, showing both the dye in the cores (dark) and surrounding them (light).

As the elliptical instability grows radially along the collision plane, the mean spacing between the cores, d, decreases linearly. However, the separation distance between the cores saturates when the perturbations deflect out-of-plane, just prior to breaking down, as shown in Fig. 2.2(C-D) and Movie S2 [48]. The minimum mean spacing between the cores is approximately equal to twice the initial core radius, σ. For the experiment, $\sigma = 0.14 \pm 0.01\,R_0$, and for the simulation, $\sigma = 0.1R_0$ (see Appendix B.2). After the elliptical instability develops and the symmetry of the two cores is broken, a periodic array of satellite flow structures is shed from each core, bridging the gap between them, as shown in the inset of Fig. 2.2(D) and Movie S3 [48]. Notably, in our experiments, the emergence of these secondary flow structures can only be resolved if the fluid outside of the cores is dyed.

2.4 Late-stage development of the elliptical instability: Secondary filaments

In order to better resolve the late-stage development of the elliptical instability and the resulting breakdown, we dye the full vortex rings, as shown in Fig. 2.3(A-F) and Movie S4 [48]. Observing the fully dyed vortex rings reveals the intricate structure of the flow that develops in response to the core dynamics. The antisymmetric coupling of the perturbations break the azimuthal symmetry of the flow, leading to the exchange of fluid between the two rings. This periodic wrapping of dye causes the outer layers of the rings to interdigitate around one another along alternating "tongues," [40] as shown in Fig. 2.3(A-B). At the boundaries of adjacent tongues, the dyed fluid curls into vortex filaments, perpendicular to the cores, as shown in Fig. 2.3(C). These alternating filaments are stretched by the circulating vortex cores into an array of counter-rotating secondary vortices, as shown in Fig. 2.3(D-E). The secondary filaments have a fleeting lifetime of only tens of milliseconds before they break down. Violent interactions between the secondary filaments and primary cores result in the rapid ejection of fine-scale vortices and the formation of a turbulent cloud, as shown in Fig. 2.3(F).
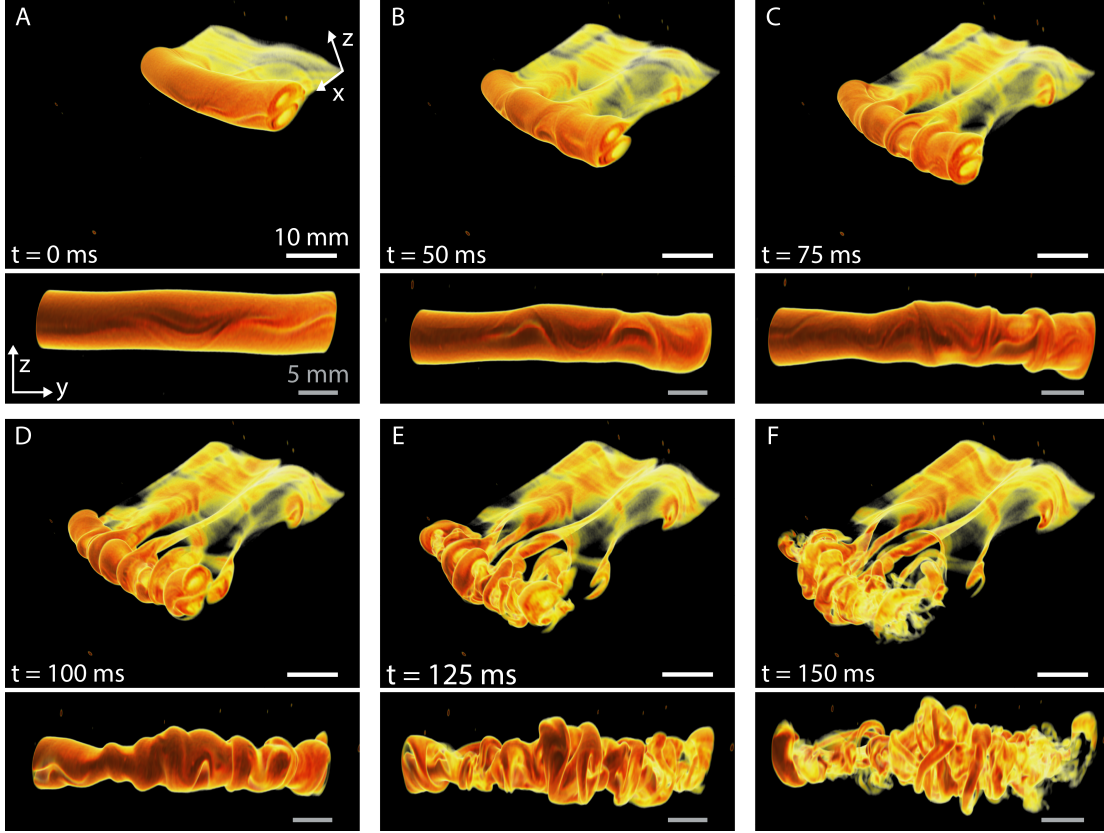
Figure 2.3: Formation of perpendicular secondary filaments in a typical experimental vortex ring collision. 3D reconstruction of two fully-dyed vortex rings colliding head-on, viewed from overhead (top) and from the side (bottom). Re = 6000 and SR = 2.5. (A-C) As the rings grow, they interdigitate as the dye from the upper ring is wrapped around the lower ring and vice-versa. (D-E) The colliding rings form an array of secondary vortex filaments that are perpendicular to the vortex cores. (F) The cores and perpendicular filaments break down into a fine-scale turbulent cloud.

By performing direct numerical simulations of the colliding vortices, we additionally probe how energy is transferred through the flow via the onset of the elliptical instability. Since the breakdown of the vortices is localized to the area around the cores, we implement a new configuration for the simulations, which consists of two initially parallel, counter-rotating vortex tubes with circulation Γ, initially spaced a distance, $b = 2.5\sigma$, apart. The flow is simulated in a cubic domain of side length, $\mathcal{L} = 16.67\sigma$, and the Reynolds number of this configuration is given by $\mathrm{Re}_\Gamma = \Gamma/\nu$ (see Appendix B.1). From PIV measurements, we find that $\mathrm{Re}_\Gamma \approx 0.678\mathrm{Re}$ as shown in Appendix B.2.

The dynamics of the vorticity distribution in the simulated flow are qualitatively equivalent to the experimental flow visualizations, as shown for a typical example at $\text{Re}_\Gamma = 4500$ in Fig. 2.4(A-C) and Movie S5 [48]. When the antisymmetric perturbations resulting from the elliptical instability materialize, the tips of the perturbed cores deform into flattened vortex sheets, as illustrated in Fig. 2.4(A). These sheets are stretched by strains applied by the other core and roll up along the edges into an alternating series of hairpin vortices, as shown in Fig. 2.4(B) and Appendix B.4.1. Upon stretching across the gap to the other perturbed core, these hairpin vortices form an ordered array of secondary vortex filaments perpendicular to the initial tubes, as shown in Fig. 2.4(C). Adjacent pairs of secondary filaments counter-rotate relative to one another [40], as shown in Fig. 2.4(D). Integrating the transverse vorticity along the symmetry plane, we find that as the secondary filaments are stretched, approximately 25% of the streamwise circulation from the initial vortex tubes is conveyed to each filament (see Appendix B.4.2). As the vorticity of the original tubes is transferred to the secondary filaments, the circulation of the flow is conserved.
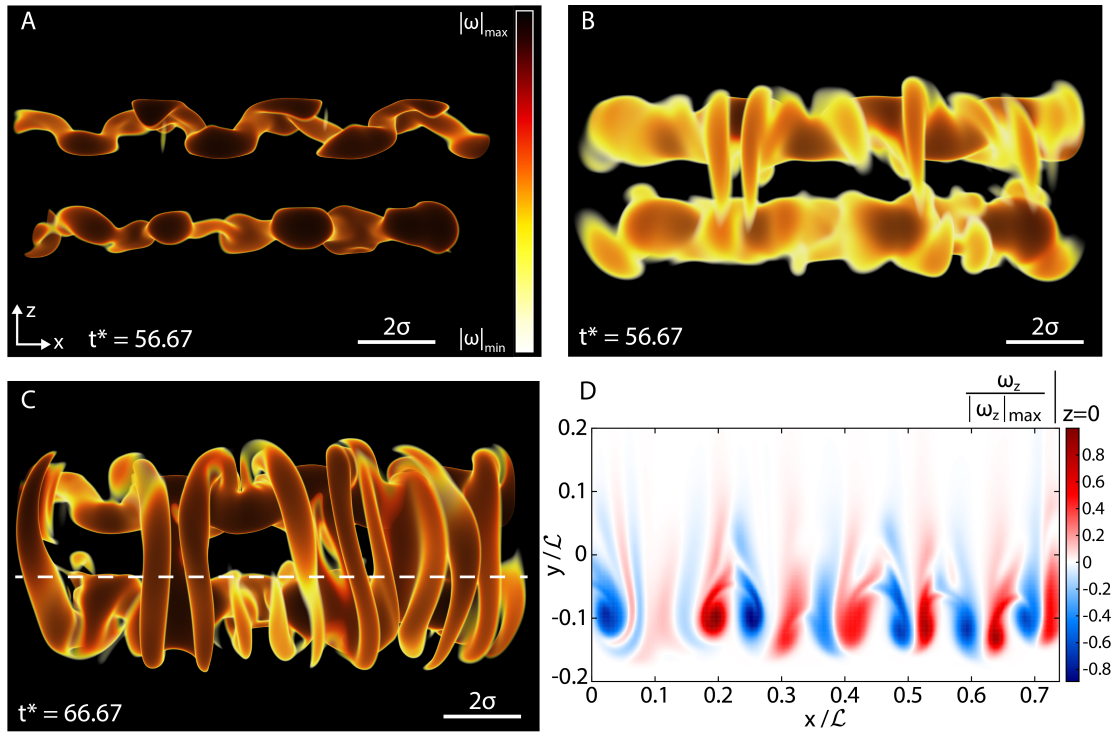
Figure 2.4: Generation of perpendicular secondary filaments in DNS. (A-C) Vorticity modulus for simulated interacting tubes where $\text{Re}_\Gamma = 4500$, $\sigma = 0.06\mathcal{L}$, $b = 2.5\sigma$, and $t^* = \Gamma t/b^2$. The vorticity modulus is normalized by the maximum vorticity modulus during the simulation, $|\omega|_{max}$. (A) The initial antisymmetric perturbations of the cores develop as the tips of the perturbations locally flatten ($0.103 \leq |\omega|/|\omega|_{max} \leq 0.117$). (B) At the same time, low-vorticity perpendicular filaments form as a result of the perturbations ($0.046 \leq |\omega|/|\omega|_{max} \leq 0.092$). (C) Once the secondary filaments form, their vorticity amplifies ($0.076 \leq |\omega|/|\omega|_{max} \leq 0.114$). (D) Vorticity distribution in the z-direction along the center plane ($z = 0$) indicated by the dashed line in (C). Adjacent secondary filaments counter-rotate.

36

2.5 Interactions of secondary vortices

Once formed, each pair of secondary filaments can be locally viewed as a replica of the initial flow configuration on a smaller scale and with a reduced circulation, hence corresponding to a smaller effective Reynolds number. The resulting close-range interactions of neighboring filaments can lead to an iterative cascade by which even more generations of small-scale vortices are formed. For collisions at moderately high Reynolds numbers (e.g. $Re_\Gamma = 3500$), the concentrated strains exerted by the counter-rotating secondary filaments cause one of them to flatten into an extremely thin vortex sheet and split into two smaller tertiary vortex filaments, as shown in Movies S6-S7[48] and Appendix B.5. This behavior is consistent with the breakdown mechanism observed experimentally in the head-on collision of vortex rings at comparatively lower Reynolds numbers mediated by the Crow instability[45].

In the high-Reynolds number limit, the secondary filaments may give rise to another generation of perpendicular tertiary vortex filaments, as shown for a typical example at $Re_\Gamma = 6000$ in Fig. 2.5(A-F) and Movies S8-S9[48]. The secondary filaments are drawn into one another due to their mutual counter-rotation, as shown in the close-ups in Fig. 2.5(B-C). The narrow gap between these writhing vortices, which experiences intense strain, almost instantaneously becomes enveloped by several high-vorticity tertiary filaments, as shown in Fig. 2.5(D-E). These tertiary filaments align perpendicular to the previous generation of vortices, wrapping tightly around them. The tertiary filaments develop locally in an ordered manner while the remnants of the primary cores and secondary filaments become increasingly entangled into a disordered "soup" of vortices, as shown in Fig. 2.5(F).

Figure 2.5 *(following page)*: The development of a turbulent cascade. (A-F) Vorticity modulus for simulated interacting tubes where $\mathrm{Re}_\Gamma = 6000$, $\sigma = 0.06\mathcal{L}$, $b = 2.5\sigma$, and $t^* = \Gamma t/b^2$. Each panel shows the front view of the full cores (left) and a close-up top view of the interacting secondary filaments indicated in the full view (right). (A) The antisymmetric perturbations of the cores develop. (B) Perpendicular secondary filaments form between the cores. (C) Secondary filaments begin to interact with each other and break down. (D) Tertiary filaments begin to form perpendicular to the secondary filaments. (E) Tertiary filaments are fully formed. (F) The flow breaks down into a disordered tangle of vortices. The vorticity thresholds are $0.079 \leq |\omega|/|\omega|_{\mathrm{max}} \leq 0.099$ for (A) and $0.110 \leq |\omega|/|\omega|_{\mathrm{max}} \leq 0.211$ for (B-F), where $|\omega|_{\mathrm{max}}$ is the maximum vorticity modulus for the entire simulation. (G) Normalized shell-to-shell energy transfer spectra indicate whether a mode is an energy source ($T(k) < 0$) or sink ($T(k) > 0$). At early times ($t^* = 65.56, 74.44$), the secondary filaments switch from energy sinks to sources as they are generated and then interact to form new vortices. At late times, the spectra flatten as energy is transferred more uniformly across the scales of the flow. (G, inset) Normalized kinetic energy dissipation rate as a function of time. The energy dissipation rate increases with the development of the secondary filaments and peaks as the secondary filaments and residual cores break down into a tangle of fine-scale vortices. (H) Normalized kinetic energy spectra show the rapid development of a sustained turbulent state with Kolmogorov scaling–as indicated by the black line–around the peak dissipation rate.

Figure 2.5: (continued)

39
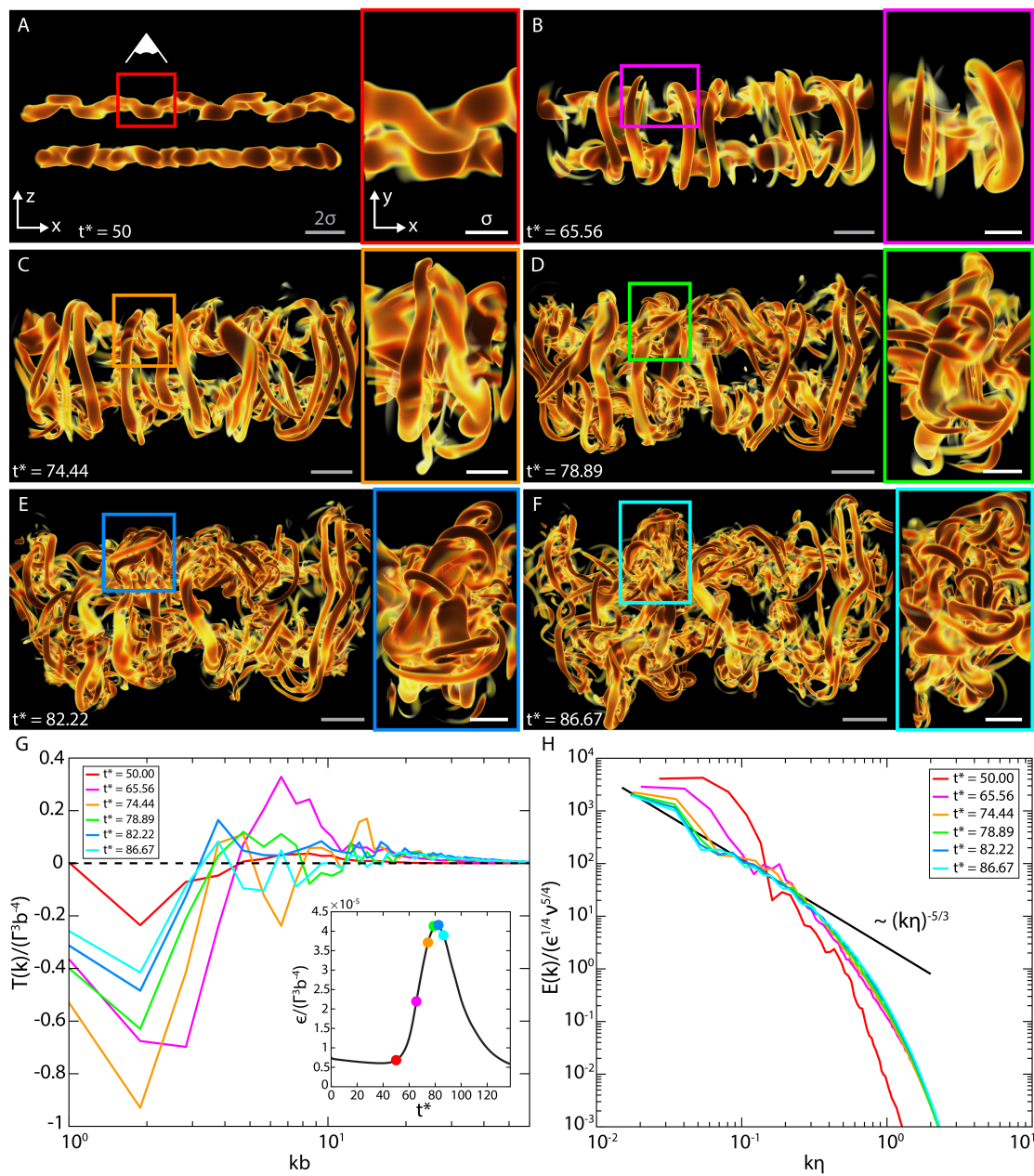
The iterative breakdown process occurs over diminutive length scales and fleeting time scales. This rapid generation of small-scale vortices leads to a dramatic increase in the energy dissipation rate, ε, as shown in the inset of Fig. 2.5(G). The initial increase in ε is triggered by the onset of the elliptical instability and the formation of antisymmetric perturbations in the cores. The following precipitous rise in the dissipation rate coincides with the formation of the perpendicular secondary filaments.

The rate at which kinetic energy is transferred across scales is calculated for the simulation in three-dimensional Fourier space through the instantaneous shell-to-shell energy transfer spectrum, $T(k, t)$, as shown in Fig. 2.5(G) [57,42]. At a fixed time, $T(k)$ is positive for a wavenumber, k, when energy flows toward the corresponding spatial scale ($\sim k^{-1}$). Conversely, a negative value of $T(k)$ indicates the flow of energy away from that corresponding spatial scale to other modes (see Appendix B.6 for details). When initially formed, the secondary filaments become pronounced energy sinks, given the large positive value of $T(k)$ at the intermediate wavenumber of approximately $kb = 6.75$. This coincides with their absorption of energy from the primary vortex cores. Next, as the secondary filaments become fully developed and interact with each other, they change behavior and become sources of energy, as indicated by the negative value of $T(k)$. Coupled with the simultaneous increase in the dissipation rate, this change in behavior of the secondary filaments from energy sinks to energy sources indicates the existence of a cascade by which kinetic energy is conveyed to smaller scales.

Through the breakdown of the secondary filaments and residual vortex cores into a disordered tangle of vortices, the dissipation rate reaches a maximum value. At this point, the flow is most vigorous and the energy transfer spectra asymptote toward a flattened profile, indicating that energy is conveyed more uniformly across the various scales of the system, as shown in Fig. 2.5(G).

Thus, for this brief time, ε maintains an approximately constant maximum value, as the energy is smoothly transferred to the smallest, dissipative scale, $\eta = \varepsilon^{-\frac{1}{4}}\nu^{\frac{3}{4}}$. Kolmogorov proposed that for turbulent flows under similar conditions, the kinetic energy spectrum follows a distinct scaling of $(k\eta)^{-5/3}$ [34]. Strikingly, we find that the fully developed turbulent cloud formed by the collision of the two vortices, indeed, exhibits Kolmogorov scaling. The evolution of the normalized energy spectra, $E(k)/(\eta^{\frac{1}{4}}\nu^{\frac{5}{4}})$, demonstrates how the flow reaches a sustained turbulent state around the peak dissipation rate, as shown in Fig. 2.5(H). This turbulent energy spectrum scaling at the peak dissipation rate also emerges during the breakdown of interacting vortex tubes mediated by the elliptical instability at lower Reynolds numbers, as shown in Appendix B.7.1. Since the energy input of the system is finite, this turbulent state cannot be maintained indefinitely. As time progresses further, the viscosity of the fluid damps out the motion of the vortices at the smallest scales. While much energy remains at the large scales of the flow, it is unable to be transmitted to smaller scales following this iterative breakdown. Accordingly, the energy dissipation rate decreases and the turbulent state decays.

2.7 DISCUSSION

The violent interaction between two counter-rotating vortices leads to the rapid emergence of a turbulent cascade, resulting in a flow with an energy spectrum that—for an ethereal moment—obeys Kolmogorov scaling. We find that the emergence of this turbulent cascade is initiated by the late-stage, nonlinear development of the elliptical instability, which forms an ordered array of counter-rotating secondary vortex filaments perpendicular to the primary cores. In the high-Reynolds number limit, the neighboring secondary filaments may interact to form a new generation of perpendicular tertiary vortex filaments. These interactions of the secondary filaments with each other and the remnants of the vortex cores lead to the rapid formation of small-scale vortices. This ensemble

of vortices interacting over the full range of scales of the system provides a conduit through which energy cascades down to the dissipative scale.

The iterative cascade, which leads to the generation of vortices at decreasingly small length scales, is strongly reminiscent of the mechanism proposed by Brenner, Hormoz, and Pumir[6]. One may speculate that the self-similar process suggested by this work could be modeled by assuming, in the spirit of[6], that at each iteration, the circulation is multiplied by a factor $x_\Gamma < 1$, and the characteristic scale of the vortices by a factor $x_\delta < 1$, resulting after n steps in a generation of vortices with circulation, $\Gamma_n = x_\Gamma^{n-1}\Gamma_1$, and a spatial scale, $\delta_n = x_\delta^{n-1}\delta_1$. The corresponding time scale over which each step evolves can be estimated as $t_n \sim \delta_n^2/\Gamma_n \sim (\delta_1^2/\Gamma_1)\,(x_\delta^2/x_\Gamma)^{n-1}$. The cascade can go all the way down to vanishingly small spatial scales in a finite time provided $x_\delta^2 < x_\Gamma$. The numerical results presented here, during the first steps of the cascade, suggest that $x_\Gamma \sim 0.25$, and $x_\delta \sim 0.2 - 0.4$, and therefore that the cascade may proceed in a finite time. It would be interesting to understand whether the cascade suggested by this work proceeds faster or slower than the Kolmogorov cascade. Whereas Kolmogorov theory implies $t_n/t_1 \sim (\delta_n/\delta_1)^{2/3}$ [16], our results imply that $t_n/t_1 \sim (\delta_n/\delta_1)^{2-\ln(x_\Gamma)/\ln(x_\delta)}$. Therefore, the cascade proposed in this work proceeds faster than the Kolmogorov cascade for $x_\delta < x_\Gamma^{3/4}$. Our estimates suggest that the two cascades may proceed asymptotically at a comparable rate. A more precise understanding of the development of the elliptical instability is necessary to determine accurately the scaling factors x_Γ and x_δ.

The essential element of the cascade process is that at each scale, discrete pairs of antiparallel vortices are able to locally interact and produce a subsequent iteration via the elliptical instability. Vortices of similar size and circulation locally align in an antiparallel manner when they interact. This is a well established consequence of Biot-Savart dynamics[72]. Thus, the largest strains that drive the cascade will arise from the interactions of nearby vortices. we suggest that iterations of this cascade could proceed down to ever-smaller scales until viscous effects take over. Yet, the proliferation of other small-scale vortices, clearly visible in Fig. 5, could conceivably prevent vortex pairs from form-

ing at some stage of the process, and we do not rule out that it may influence the dynamics. We remark, however, that the present work shows that only two clear iterations of the cascade are sufficient to produce a Kolmogorov spectrum. Even in the high-Reynolds number limit, a finite set of iterations occurring simultaneously for many independent pairs of interacting vortices might suffice to establish and sustain a turbulent cascade. The details of how this iterative process unfolds in the limit of large Reynolds number is an important question for future research.

This framework strongly agrees with recent works by Goto et al. in a fully turbulent flow regime. Namely, their numerical results demonstrate the existence of many independent pairs of antiparallel vortices interacting and locally forming smaller generations of perpendicular vortex filaments in both fully developed homogeneous isotropic turbulence and wall-bounded turbulence [19,20,54]. These discrete interactions of antiparallel vortex pairs appear simultaneously throughout Goto's simulations over four distinct scales [20]. Due to the striking similarities between the iterative mechanism we observe and the results of Goto, we propose that the elliptical instability is likely the means by which these successive generations of perpendicular filaments are formed. Establishing a precise connection between our own results and Goto's observations requires a fully quantitative analysis, which is beyond the scope of the present work.

Our work thus demonstrates how the elliptical instability provides a long-sought-after mechanism for the formation and perpetuation of the turbulent energy cascade through the local interactions of vortices over a hierarchy of scales. Supplied by the injection of energy at large scales, discrete iterations of this instability effectively channel the energy of a flow down to the dissipative scale through the formation of new vortices. From a quantitative point of view, the approximate estimates provided in this work suggest that the corresponding cascade proceeds in a finite time, although a precise comparison with the Kolmogorov cascade requires a better understanding of the nonlinear development of the elliptical instability. While the dynamics of turbulent flows likely involve other multi-scale vortex interactions, this fundamental mechanistic framework can begin to

unravel the complexity that has long obscured our understanding of turbulence.

2.8 Acknowledgements

3

Conclusion

The dynamical evolution of turbulence is mired in complexity that arises from the intricate 3D motion of interacting vortices over a wide range of length and time scales. Statistical approaches have been utilized to obscure the details of these vortex interactions in order to characterize the overall, emergent behavior of turbulent flows. However, our understanding of how turbulence develops will remain limited as long as we continue to use statistical methods to abstract away how these ensembles of interacting vortices convey the energy of the flow down to dissipative scales.

In this thesis, we have begun to examine the mechanistic underpinnings of the turbulent energy cascade; that is, we have investigated through what real-space configurations counter-rotating vortices interact with each other and break down to small scales. We have shown that the head-on collision of vortex rings provides an excellent case study in measuring and characterizing the mechanistic "building blocks" that lead to the formation of a transient turbulent flow. At moderate Reynolds numbers, the breakdown is mediated by the Crow instability, in which the interacting vortices locally contact, flatten, and split into a new, smaller generation of vortex filaments (Chapter 1). At high Reynolds numbers, the breakdown is driven by the onset of the elliptical instability, which gives rise to an array of counter-rotating secondary filaments, perpendicular to the original colliding vortices (Chapter 2). Successive iterations of these breakdown modalities have also been observed, suggesting the possible extensibility of these "building blocks" to other, more general turbulent flow configurations. The application of these local breakdown mechanisms to the complicated dynamics of HIT poses many challenges, as there are likely other latent mechanisms by which vortices at a large scales interact with smaller vortices. Nonetheless, these tools could help advance our understanding of turbulence in a more fundamental, bottom-up manner, enabling us to analyze turbulence as a cascade of discrete vortex interactions, rather than statistically.

Supplementary Material: Chapter 1

A.1   EXPERIMENTAL SETUP AND PROCEDURE

Two identical vortex rings are launched head-on into one another in a 75-gallon water aquarium ($45 \times 122 \times 50$ cm^3). The vortex rings are formed using two piston-cylinder assemblies, as shown in Fig. A.1. Each piston is driven by an underwater linear shaft motor (Nippon Pulse S160D) through a stainless steel tube with a diameter, $D = 2.54$ cm, expelling a slug of fluid of length, L, through

the tapered nozzle. The pistons are impulsively accelerated to a constant speed, $U \leq 1$ m/s. The displacement of both pistons is measured with a non-contact linear encoder (Renishaw LM15) with a resolution of 5 μm. The linear motors are servo controlled and coupled with each other through CNC software (TwinCAT3) so that the firing of the vortex rings is synchronized. Each vortex cannon is capable generating vortex rings with a maximum Reynolds number, Re $= UD/\nu$, of 25,000, where ν is the kinematic viscosity of water, and a maximum stroke ratio, SR $= L/D$, of 4[18]. The outer orifice of the vortex cannon is double-walled, and fluorescent dye (Rhodamine B) is ejected through the thin, 150 μm, gap just prior to firing the pistons, as shown in Fig. A.1 (b)[67]. As the ejected fluid separates at the sharp edge of the nozzle, the ring of dye becomes trapped in the core of the vortex, allowing us to visualize the dynamics of the vortex cores.

In all the experiments discussed in this work, the vortex cannons are spaced a distance, $H = 8D$, apart. We simultaneously fire two identical vortex rings head-on into each other. As the counter-rotating vortex rings initially approach one another, they expand radially and become flattened along the collision plane, as shown in Fig. 1.2 in the main text. We directly observe the breakdown dynamics of the vortex rings in real-time and in 3D by imaging the flow tomographically with a scanning laser sheet. Recently, Irvine et *al.* used a similar visualization technique to measure various properties of coherent vortices in 3D[33,68]. They developed a powerful method to recover the flow field of the vortices by mapping the centerlines of the vortex cores, but this required that the cores remain largely undeformed. The dynamics of our system involve extreme contortions and deformations of the vortex cores, which cannot be captured by merely resolving the centerlines of the vortices. Studying this rapid breakdown requires clearly resolving the full three-dimensional structure of the vortex cores.

The collision plane is illuminated by a pulsed ($\approx$ 15 ns), 2-Watt laser sheet (Spectraphysics Explorer One 532-2W), which is synchronized with the exposure signal of a high-speed imaging sensor (Phantom V2511), as shown in Fig. 1.1 (b-c) in the main text. The laser beam is deflected by a mir-
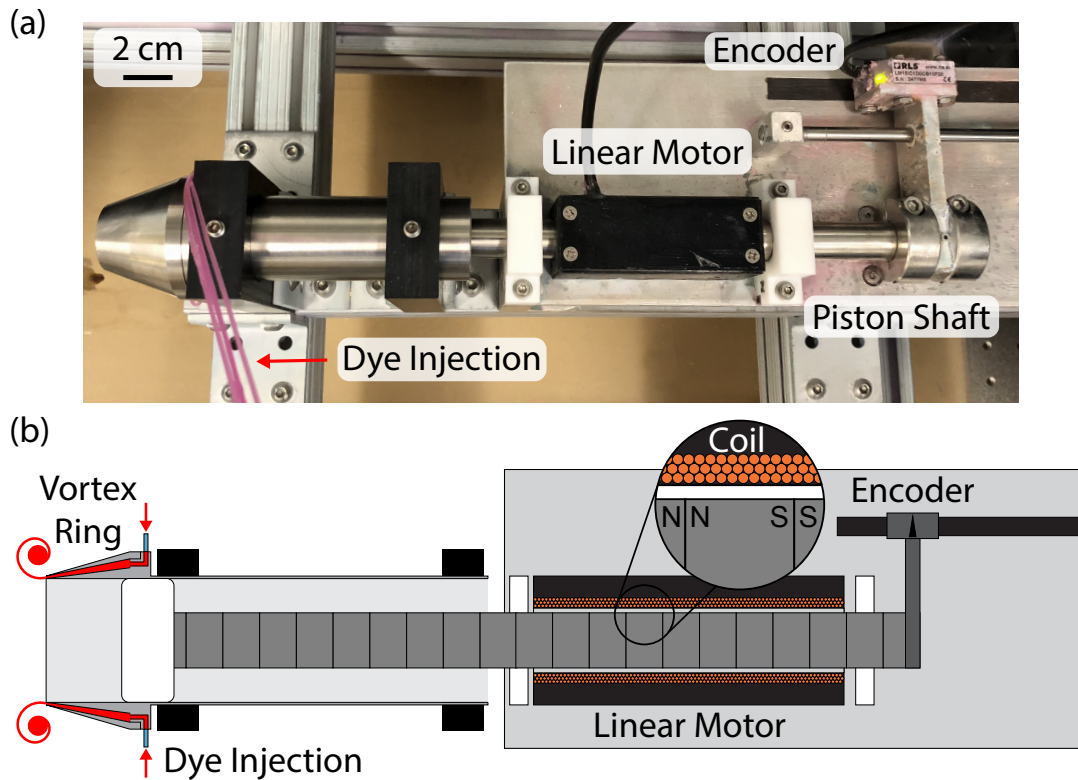
Figure A.1: Vortex cannon assembly. (a) Image and (b) cross-sectional schematic of the vortex cannon assembly. The piston shaft is loaded with permanent magnets and is impulsively driven by the magnetic fields generated by a series of current-carrying coils in the linear motor. The linear motor is servo controlled, and the feedback position of the piston is measured by a non-contact linear encoder. The core of the vortex ring is dyed by injecting fluorescent dye at the outer edge of the nozzle.

ror mounted on a servo-controlled galvanometer (Cambridge Technology Model 6210HM60), which is placed at the focal point of a plano-convex lens; thus, the deflected beam is collimated. The laser beam then passes through a cylindrical lens that opens into laser sheet with a thickness of 100 μm. The laser sheet scans over a distance of up to 2.54 cm at a frequency of 1 kHz, driven via a sawtooth command signal. At this rapid scanning rate, the flow is effectively "frozen" during each scan. The high-speed camera captures cross sections of the flow illuminated by the laser sheet as it scans through the fluid. A sequential series of 2D image slices is thus continuously captured by the

high-speed camera. High-intensity regions in these image slices correspond to the fluorescent dye within the vortex cores. The short pulsing of the laser is critical to prevent the blurring of the images due to the motion of the laser sheet. The dynamics described in this paper cannot be observed with a continuous laser.

The timing of each captured image is correlated with the measured position of the laser sheet. Each stack of 2D image slices is reconstructed into a 3D volume with dimensions of $256 \times 384 \times 114$ voxels using Dragonfly visualization software (Object Research Systems). The reconstructed 4D data has a resolution of ($145 \times 145 \times 100 \, \mu m^3$ and 1 msec) in the (x, y, z) directions and time. The resolution of the volume in the xy-plane is limited by the magnification of the lens on the high-speed camera (Nikkor f= 85 mm, f/1.4), and the resolution in the z-direction is given by the spacing between the image slices and the thickness of the laser sheet. This imaging technique allows us to directly observe and probe the full volume and resolve the three-dimensional dynamics of the vortex ring collision with high spatial and temporal resolution.

A.2 VORTEX CORE TRACKING WITH PIV AND DYE

Complementary PIV measurements were conducted in order to determine how well the fluorescent dye tracks the motion of the vortex cores during the head-on collision. A laser sheet was used to illuminate a 2D cross-section aligned along the central axes of the vortex cannons, perpendicular to the collision plane. Additionally, the aquarium was seeded with polyamide particles with a diameter of $50 \, \mu m$ and a density of 1.03 g/mL (Dantec Dynamics). Several vortex ring collisions, where Re=4000 and SR=2.5, were imaged with a high speed camera using a window size of 800×1280 at a maximum frame rate of 2000 fps with a resolution of 0.14 mm/pixel. The velocity field along this 2D cross-section was evaluated using the MATLAB program PIVsuite. The locations and sizes of the vortex cores were then detected by fitting the vorticity distribution of each core to a two-
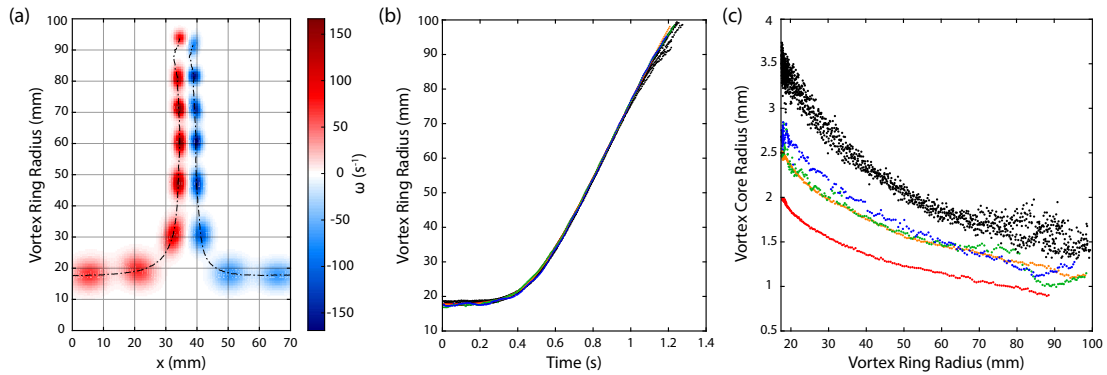
Figure A.2: Vortex core tracking in 2D with PIV and dye. (a) Vorticity distribution and core trajectory of two colliding vortex rings at several time steps obtained via PIV through a 2D cross section perpendicular to the collision plane. The plotted vorticity distribution is the result of fitting the raw vorticity data to a 2D Gaussian function for each core. As the vortex rings collide, they grow radially and the cores contract, amplifying their vorticity before breaking down. The time steps correspond to t=0, 0.225, 0.5, 0.675, 0.8, 0.9, 1, and 1.25 s, and for all data in this figure Re = 4000 and SR = 2.5. (b) Vortex ring radius vs. time for 10 collisions where the vortex core is tracked from the vorticity data via PIV (black) and from the dyeing the core with fluorescent dye (color). (c) Vortex core radius vs. vortex ring radius for 10 collisions; the core is tracked by fitting to the vorticity data (black) and by injecting the vortex ring with various amounts of fluorescent dye: 0.08 mL (red), 0.1 mL (orange), 0.1 mL (green) and 0.12 mL (blue).

dimensional Gaussian function, as shown in Fig. A.2(a). When the vortex rings collide, they grow radially in an axisymmetric manner, amplifying the vorticity of the core through vortex stretching, before developing perturbations and breaking down, as shown in Fig. 1.2 in the main text.

Additionally, the same collisions were performed and visualized along this illuminated 2D plane with one of the vortex cores dyed using fluorescent dye (Rhodamine B). The cross-section of the dyed core was segmented and fitted to an ellipse in order to extract the centroid of the core, its semi-major axis length, a, and its semi-minor axis length, b. The trajectories of the colliding vortex cores follow the same linear trend of radial growth for both the cores tracked with vorticity through PIV and through dyeing the core, as shown in Fig. A.2(b). The vortex core radius was calculated as the average of the standard deviation in the two principal directions for the cores fitted from the vorticity data and the average of a and b for the dyed cores. During the radial growth of the rings when they collide, the vortex cores accordingly contract due to vortex stretching, as shown by Fig. A.2(c).

Naturally, the more dye that is initially injected into the vortex ring, the thicker the core appears throughout the collision. The radius of the dyed core is smaller than that of the core obtained from the vorticity distribution during each stage of the collision. However, for vortex rings injected with at least 0.1 mL of dye, during the later stages of the collision just prior to breakdown—i.e. when the 3D visualizations begin—the core radius from the dye under-estimates the core radius from the vorticity by less than 0.4 mm. This demonstrates that fluorescent dye effectively tracks the motion of the vorticity distribution of the core, especially when the visualized breakdown dynamics of the core begin.

A.3   Numerical Simulation Details

The incompressible Navier-Stokes equations are solved using an energy-conserving second-order centered finite difference scheme in cylindrical coordinates with fractional time-stepping. A third order Runge-Kutta scheme is used for the non-linear terms and a second order Adams-Bashworth scheme is used for the viscous terms[80]. The solver uses $q_r = r v_r$ as a primitive variable to avoid singularities near the center axis. The time-step was dynamically chosen so that the maximum Courant-Friedrich-Lewy (CFL) condition number was 1.2. A Gaussian (Lamb-Oseen) velocity profile was used as the initial condition for the velocities inside the ring with a slenderness of $\Lambda = \sigma/R = 0.35$, where σ is the core radius and R is the vortex ring radius. The Reynolds number based on the circulation, Re_Γ, is $\mathrm{Re}_\Gamma = \Gamma/\nu = 3500$, where Γ is the circulation of the vortex ring. Length and time-scales are matched to the experimental values by using the ring diameter and circulation. The first is matched by assuming the ring diameter coincides with the vortex cannon tube diameter, and the second is matched by using the piston stroke length, the piston velocity, and the correlations developed by Gharib & Shariff[18]. A passive tracer, corresponding to a dye, is also simulated. Due to computational restrictions, the Schmidt number of the dye is limited to unity.

The rings are initially positioned at a distance $L_z = 2.5R$ away from each other. A rotational symmetry, n_{sym}, of order five was forced on the simulation to reduce computational costs. The ring's initial position was perturbed according to the formula $R(\theta) = R_0 \left(1 + \varepsilon \sin \left(k[\theta + \theta_0]\right)\right)$, where ε is taken from a normal distribution with variance of 10^{-2} for the first two wavelengths, to account for the ring's self-instability, and 10^{-3} for the other wavelengths; θ_0 is taken from a uniform distribution.

The cylindrical computational domain was bounded by stress-free walls at a sufficient distance not to affect the dynamics of the flow. In practice, we set the walls at a distance R, below and above the initial locations of the vortex rings, and at a distance of $5R$ from the ring axis in the radial direction. Points were clustered near the collision plane in the axial direction, while uniform resolution was used in the other two directions. A total of $384 \times 512 \times 264$ grid points were used in the azimuthal, radial and axial directions, respectively. Resolution adequacy was checked by monitoring that the viscous dissipation and the energy balance are within the acceptable bound of 1%[79].

A.4 Vorticity Evolution in Simulations

The evolution of the vorticity in the simulated collision was quantified to complement the experimental results. Fig. A.3(a) shows the amplification of the maximum and mean vorticity modulus during the collision. While the vorticity locally grows by over a factor of five, the mean vorticity never grows beyond 1.5 times its original value. This is because, as shown in Fig. 1.5, not all regions of the ring undergo the iterative evolution shown in Fig. 1.6(b).

Additionally, Fig. A.3(b) shows how the initially coherent vortex cores, whose mean vorticity is primarily aligned in the azimuthal, or $\hat{\theta}$ direction, become more three-dimensional during the late stages of the collision, as suggested by the experimental observations. Indeed, an isotropic vorticity distribution corresponds to $|\omega_\theta|/|\omega|$ of $1/\sqrt{3} \approx 0.577$, very close to the value attained at the end of

the simulation. This demonstrates that as time progresses, the flow becomes fully three dimensional and quasi-isotropic.

(a)

(b)
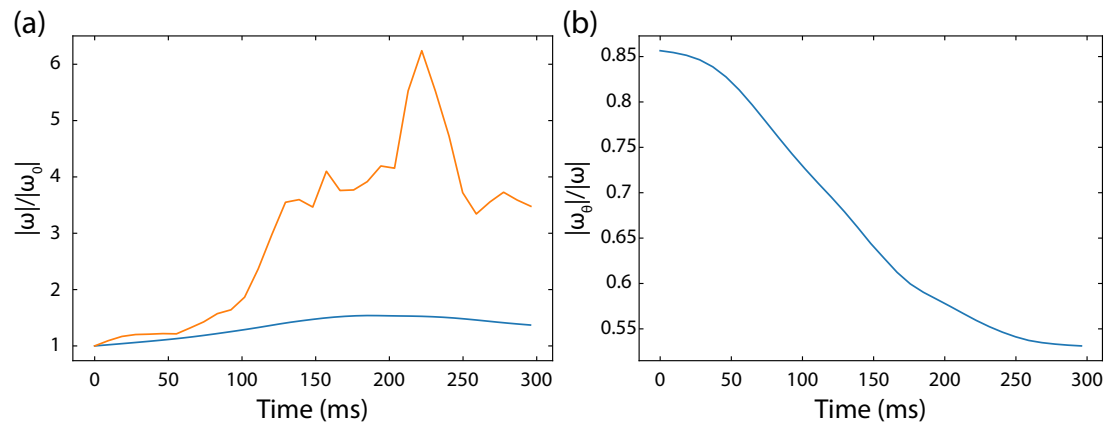
Figure A.3: Vorticity evolution in the collision simulations. (a) Evolution of the maximum (orange) and mean (blue) vorticity modulus with time, relative to the initial values. (b) Weight of the mean azimuthal component of vorticity relative to the mean vorticity modulus as a function of time. A value of $1/\sqrt{3} \approx 0.577$ would correspond to a vorticity distribution with no preferential direction.

B

Supplementary Material: Chapter 2

B.1 Methods and materials

We use both experiments and simulations to probe the dynamic formation of the turbulent cascade resulting from the interaction between counter-rotating vortices. Experimentally, we examine the head-on collision of vortex rings, and numerically we examine the collision of vortex rings and vortex tubes. In the experiments[45], fluorescent dye (Rhodamine B) is injected into the initially formed

rings to visualize the core dynamics, as shown in Fig. 2.1(A) in the main text. Two vortex rings are fired head-on into one another in a 75-gallon aquarium. The vortex cannons are positioned a distance of $8D$ apart, where D is the vortex cannon diameter. The full, three-dimensional dynamics of the resulting collision are visualized by tomographically scanning over the collision plane with a rapidly translating pulsed laser sheet ($\lambda = 532$ nm). The pulsing of the laser (Spectraphysics Explorer One 532-2W) is synchronized with the exposure signal of a high speed camera (Phantom V2511), which images the illuminated plane head-on. Each image plane spans along the xy-plane, and the laser sheet scans in the z-direction. Thus, for each scan, the image slices are stacked together to form a 3D reconstruction of the collision. The spatial resolution of each volume is $145 \times 145 \times 100$ μm^3 per voxel in (x,y,z), and the time resolution is up to 0.5 ms per scan. The number of voxels in each scanned volume depends on the imaging window size, the camera frame rate, and the scanning rate. For example, the volume size is $512 \times 512 \times 64$ voxels in (x, y, z) for the dyed core collision in Movie S2 and $384 \times 288 \times 75$ voxels for the fully dyed ring collision in Movie S4. The series of volumetric scans are reconstructed in full 3D with temporal evolution using Dragonfly visualization software (Object Research Systems). The imaging apparatus can only detect the dyed regions of the fluid, so any flow structures that emerge during the breakdown that are undyed cannot be observed. When only the vortex cores are dyed, we probe through the volumes of each 3D scan along the azimuthal direction to locate the centroids of the cores at each cross section. This enables us to extract the vortex core centerlines, which we use to track the deformation of the cores and measure the vortex ring radius, $R(t)$, and the average spacing between the cores, $d(t)$. In order to visualize the development of secondary flow structures that emerge during the collisions, we fill the vortex cannons with fluorescent dye prior to driving the pistons to form the rings. As a result, the regions around the vortex cores are dyed, as shown in Fig. 2.3 in the main text.

We use direct numerical simulations (DNS) to further probe the unstable interactions between the vortices. This allows us to directly examine the evolution of the vorticity field, relate it to ex-

perimental visualizations, and compute statistical quantities characterizing the flow. We solve the incompressible Navier-Stokes equations using an energy-conserving, second-order centered finite difference scheme with fractional time-stepping. We implement a third-order Runge-Kutta scheme for the non-linear terms and second-order Adams-Bashforth scheme for the viscous terms [32,80]. We simulate both vortex rings and tubes, in cylindrical and Cartesian coordinates, respectively. To avoid singularities near the axis, the cylindrical solver uses $q_r = rv_r$ as a primitive variable [80]. The time-step is dynamically chosen such that the maximum Courant-Friedrich-Lewy (CFL) condition number is 1.2. Resolution adequacy is checked by three methods: monitoring the viscous dissipation and the energy balance, examining the Fourier energy spectra, and using the instantaneous Kolmogorov scale. White noise is added to all all initial conditions to trigger the most unstable modes.

The rings are initialized as two counter-rotating Gaussian (Lamb-Oseen) vortices, each with a core radius σ wrapped into a torus of radius R_0. The control parameters for this system are the circulation Reynolds number, $Re_\Gamma = \Gamma/\nu$ and the slenderness ratio of the rings, $\Lambda = \sigma/R_0$. The circulation of the vortex rings, Γ, and the initial ring radius, R_0, are used to non-dimensionalize parameters in the code. We simulate the collision in a closed cylindrical domain, bounded by stress-free walls at a distance far enough to not affect the collision. After testing several configurations, the bounds on the domain were placed a distance R_0 below and above the rings, and $5R_0$ from the ring axis in the radial direction. For the simulation presented in this paper, we selected a ring slenderness of $\Lambda = 0.1$, a circulation Reynolds number of $Re_\Gamma = 4500$, and an initial ring-to-ring distance of $d = 2.5R_0$. These parameters are comparable to the experimental vortex rings, as shown by the measurements in Appendix B.2. Points are clustered near the collision regions in the axial and radial directions, while uniform resolution is used in the azimuthal direction [18,45]. A rotational symmetry of order five is forced on the simulation to reduce computational costs. The vortex core centerlines are located by slicing azimuthally through the pressure field at every time step and identifying the local minima of each vortex cross section. Additionally, a simulated passive scalar is injected into

57

the vortex rings to visualize the dynamics of the collision and compare with experiments, as shown in Movie S3. Due to computational restrictions, the diffusivity of the dye is equal to the kinematic viscosity of the fluid (i.e. the Schmidt number is unity).

For the vortex tubes, we simulate a triply periodic cubic domain of period $\mathcal{L}$, which is discretized using a uniform grid. The two counter-rotating, parallel tubes are both initialized with a Gaussian (Lamb-Oseen) vorticity profile of radius, σ, and circulation, Γ, initially separated a distance, b, apart. The system is characterized by two dimensionless parameters: the circulation Reynolds number, Re_Γ, and the ratio σ/b. Again, the circulation, Γ, is used as a non-dimensional parameter, along with b. We set the core size to $\sigma = 0.06\mathcal{L}$, fix $b/\sigma = 2.5$, and run simulations with Re_Γ at 2000, 3500, 4500, and 6000, with grid sizes of 256^3, 360^3, 540^3, and 540^3, respectively. As the counter-rotating tubes interact and break down, they naturally propagate through the periodic domain. For each visualization, the propagation of the tubes is subtracted so that the tubes remain in the center of the domain. Additionally, in all 3D visualizations of the vorticity modulus, $|\omega|(t)$, the vorticity modulus at each voxel is normalized by the maximum vorticity modulus for all time, $|\omega|(t)_{\max}$ (see Appendix B.7.2).

B.2 PIV ANALYSIS OF VORTEX RING GEOMETRY

The vortex rings are characterized experimentally through 2D patricle image velocimetry (PIV). The fluid is seeded with polyamide particles with a diameter of 50 μm and a density of 1.03 g/mL (Dantec Dynamics). A laser sheet is positioned along the central axis of the vortex cannon in order to illuminate the cross section of the ejected vortex rings. The motion of the particles in the vortex rings along this cross section is imaged with a high-speed camera (Phantom V2511) with a window size of 1280 × 800 pixels at a maximum frame rate of 2000 fps, such that the resolution is 0.12 mm/pixel. Vortex rings are formed over a range of stroke ratios (SR = L/D) and Reynolds num-

bers (Re= UD/ν), where L is the stroke of the piston, $D = 25.4$ mm is the diameter of the vortex

cannon, U is the piston velocity, and ν is the kinematic viscosity of water.

The velocity field for each generated vortex ring is calculated using MATLAB PIVsuite. The

cores of the vortex rings are identified by computing the vorticity field, and each core is fitted to

a two-dimensional Gaussian function, as shown for a typical example in Fig. B.1 and Movie S10.

After pinching off, the vortex ring reaches a steady size with radius, R_0, as it propagates forward

through the fluid, as shown in Fig. B.1(A). Additionally, the core radius, σ, is calculated by averaging

the standard deviations of each Gaussian fit, σ_x and σ_y, as shown in Fig. B.1(B).
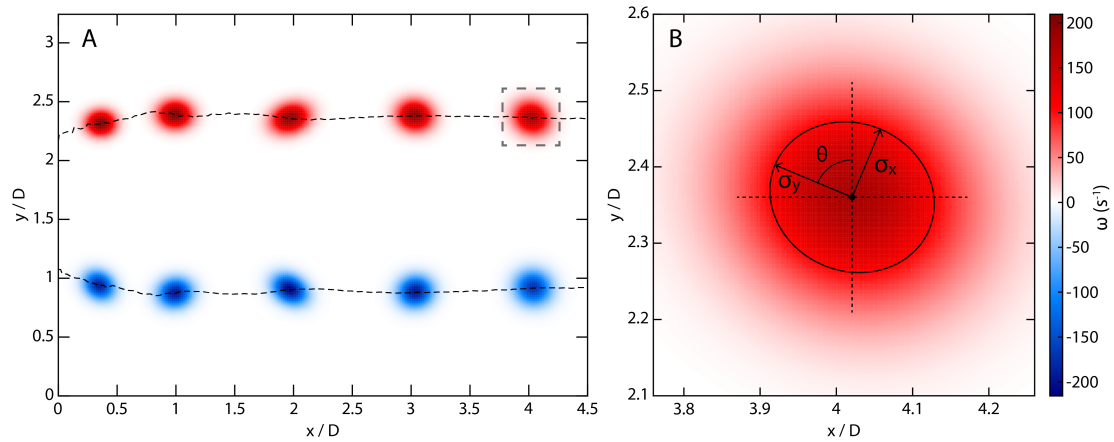
Figure B.1: Vortex ring tracking and measurement through PIV. (A) 2D vorticity distribution and core trajectories for a vortex ring formed via a piston-cylinder assembly, where Re = 7000 and SR = 2.5. Each vorticity distribution results from fitting the raw vorticity data to a 2D Gaussian function. The time steps correspond to $t =$ $0, 0.158, 0.368, 0.578,$ and 0.788 seconds, and the vortex cannon orifice is located at $x = 0$. (B) Zoomed-in view of the final vortex core indicated by the dashed gray box. The vortex core is defined by the level curve shown by the black ellipse, with a center point, $\left(\mu_x, \mu_y\right)$, a rotation angle, θ, and standard deviations, σ_x and σ_y.

By fitting to the vortex cores to a Gaussian function, we evaluate the geometry of the rings over

a wide range of Reynolds numbers at various stroke ratios, as shown in Fig. B.2. This parameteriza-

tion of the vortex rings and their core structures enables us to directly relate the initial state of the

vortex rings used in the experimental collisions to those of the simulations, as described in the main

text. Accordingly, all of the parameterizations for the vortex ring geometry are performed when the

vortex ring propagates a distance between $2D$ and $4D$ from the orifice of the vortex cannon. This corresponds to the range of distances required for the vortex ring to pinch off and reach a steady morphology prior to reaching where the collision plane is located in the experiments at $4D$.

At every stroke ratio, the core size is larger for the vortex rings produced with lower Reynolds numbers, as shown in Fig. B.2(A). However, for vortex rings with a Reynolds number greater than $\sim 10,000$, the core size remains relatively constant. This is because vortex rings formed at lower Reynolds numbers are more susceptible to viscous dissipation from the ambient fluid as they propagate forward. This dissipation leads to a spreading of the vorticity distribution in the cores through the diffusion of momentum via the viscosity of the fluid, thereby resulting in the thicker cores of the vortex rings at lower Reynolds numbers. The vortex ring radius, R_0, remains roughly constant for each stroke ratio over this wide range of Reynolds numbers, as shown in Fig. B.2(B). Like with the core size, the vortex rings formed with a larger stroke ratio naturally have a slightly larger radius, as more fluid is injected to form vortex rings. However, by normalizing the core radius with the vortex ring radius at each Reynolds number to compute the slenderness ratio, Λ, the data collapses, as shown in Fig. B.2(C). This consistency of the vortex ring and core geometry across various stroke ratios informs the selection of the vortex ring parameters in the simulated collisions described in the main text. In particular, for all of the simulated vortex ring collisions, a slenderness ratio of $\Lambda = 0.1$ is used.

The circulation of the vortex cores, Γ, is calculated by integrating the raw vorticity data for each core over an elliptical contour defined by the Gaussian fit that overcompensates the core size by a factor of 1.5 for both standard deviations. The magnitude of the circulation is then normalized by the kinematic viscosity of the fluid in order to compute the circulation Reynolds number, $\mathrm{Re}_\Gamma = \Gamma/\nu$. This parameter, as previously discussed in the main text and in Appendix B.1, is used to define the Reynolds number in the numerical simulations of the colliding vortex rings and the interacting vortex tubes. This calculation thus allows to relate the Reynolds number of the vortex rings formed
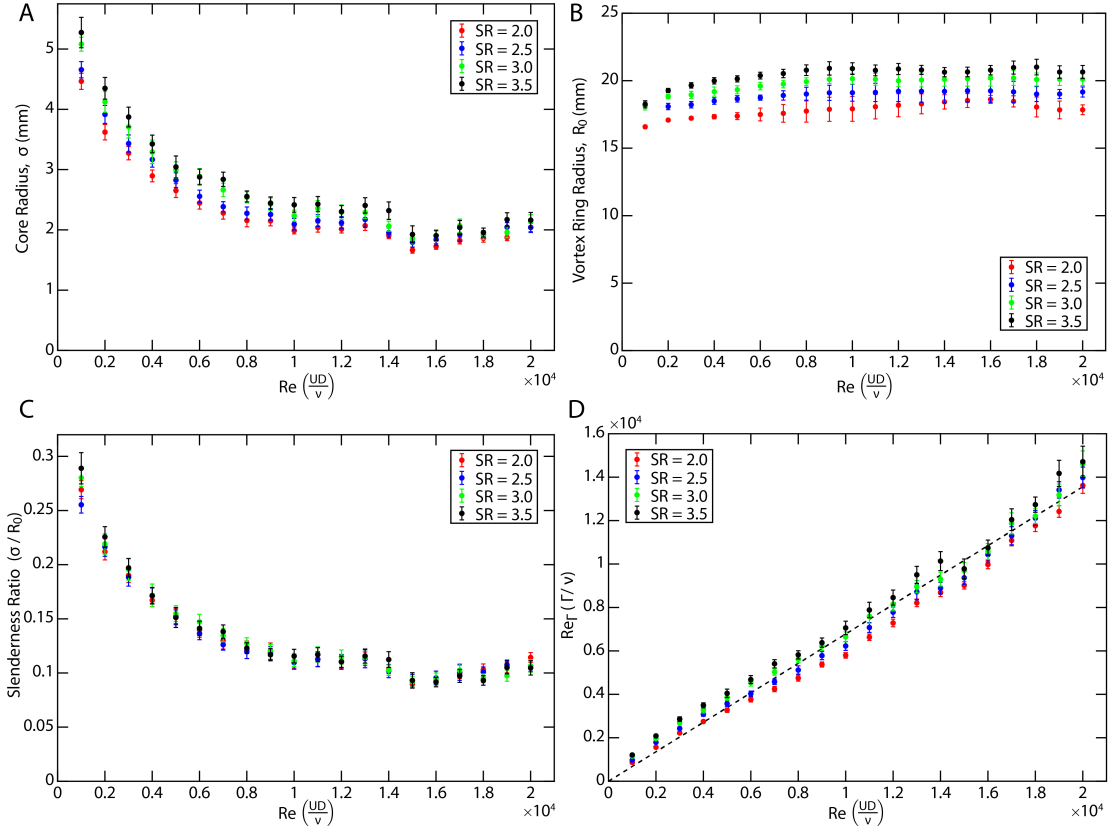
Figure B.2: Vortex ring and core geometry. From the Gaussian fits of the vorticity data, the following parameters are measured as a function of the Reynolds number across various stroke ratios: (A) vortex core radius, σ, (B) vortex ring radius, R_0, (C) slenderness ratio, Λ, and (D) circulation Reynolds number, Re_Γ. The dashed line in (D) corresponds to the linear fit to the data: $Re_\Gamma = 0.678Re$. All calculations are performed when the vortex rings reach a distance between $2D$ and $4D$ from the vortex cannon orifice.

experimentally with those formed numerically, as shown in Fig. B.2(D). Accordingly, we find that the experimental Reynolds number scales linearly with the circulation Reynolds number, such that $Re_\Gamma \approx 0.678Re$, which is consistent with previous experimental works [18].

B.3 Simulating vortex ring collisions using the Biot-Savart approximation

B.3.1 Biot-Savart model and regularization

In this section, we establish the conditions that lead to the emergence of the elliptical instability in vortex ring collisions, focusing on the range of Reynolds numbers in which this instability is observed. Our approach consists of modeling the rings using the Biot-Savart model [52,72,73] while accounting for the evolution of the core size, which is assumed to have a circular cross-section for all time. With the parameters given by this model, we determine the growth rate of the elliptical instability, as calculated in [37].

Regularization of the Biot-Savart model is required due to the logarithmic divergence of the principal integral. Here, we use the regularization used in [72,73]. Denoting $\sigma_i(t)$ as the core radius of each vortex filament, i, at time, t, we replace the Biot-Savart integral (up to a prefactor) by:

$$\frac{\partial \mathbf{r}_i(\theta, t)}{\partial t} = \sum_j \frac{\Gamma_j}{4\pi} \int_{\text{filament}_j} d\theta' \frac{\frac{\partial \mathbf{r}_j}{\partial \theta'} \times (\mathbf{r}_i(\theta) - \mathbf{r}_j(\theta'))}{[(\mathbf{r}_i(\theta) - \mathbf{r}_i(\theta'))^2 + \sigma_i(\theta)^2 + \sigma_j(\theta')^2]^{3/2}}. \tag{B.1}$$

In this configuration, we consider two filaments, with indices $i = 1$ and $i = 2$. The centerline positions of the filaments with circulation, Γ_i, are given by $\mathbf{r}_i(\theta, t)$. We start with an initially axisymmetric configuration, consisting of two counter-rotating vortex rings, perfectly aligned along the same central axis. We parametrize the centerlines of the two rings in the $(\hat{\mathbf{x}}, \hat{\mathbf{y}}, \hat{\mathbf{z}})$ directions by:

$$\mathbf{r}_1(\theta, t) = \begin{pmatrix} R(t)\cos(\theta) \\ R(t)\sin(\theta) \\ -d(t)/2 \end{pmatrix} \quad \text{and} \quad \mathbf{r}_2(\theta, t) = \begin{pmatrix} R(t)\cos(\theta) \\ R(t)\sin(\theta) \\ +d(t)/2 \end{pmatrix}, \tag{B.2}$$

where $R(t)$ is the vortex ring radius, and the azimuthal angle is given by $0 \leq \theta \leq 2\pi$. The perpendicular distance between the two rings, $d(t)$, is taken to be positive, and the circulations are

$\Gamma_1 = -\Gamma_2 = \Gamma > 0$. With these conventions, filament 1, at $z = -d(t)/2$, moves upward, toward filament 2 at $z = d(t)/2$.

In the following, as was the case in [72,73], we impose incompressibility, by enforcing that the total volume of the rings is conserved:

$$R(t)\sigma^2(t) = R_0\sigma_0^2. \tag{B.3}$$

The evolution equations reduce to two simple ordinary differential equations for $R(t)$ and $d(t)$, as explained in turn. With the parameterization proposed in Eq. (B.2), an elementary calculation shows that the contribution of the filament 1 to the velocity at the point $\mathbf{r}_1(\theta)$ reduces to a uniform velocity in the positive z-direction:

$$v_z^{1,s} = \frac{\Gamma}{4\pi} \int_0^{2\pi} d\theta' \frac{R(t)^2(1 - \cos(\theta - \theta'))}{[2R(t)^2(1 - \cos(\theta - \theta')) + 2\sigma^2]^{3/2}}. \tag{B.4}$$

The contribution of filament 2 to the velocity of filament 1 consists of a component in the radial direction:

$$v_r^{1,m} = \frac{\Gamma}{4\pi} \int_0^{2\pi} d\theta' \frac{d(t)R(t)\cos(\theta - \theta')}{[2R(t)^2(1 - \cos(\theta - \theta')) + d(t)^2 + 2\sigma^2]^{3/2}} \tag{B.5}$$

and a component in the vertical direction:

$$v_z^{1,m} = -\frac{\Gamma}{4\pi} \int_0^{2\pi} d\theta' \frac{R(t)^2(1 - \cos(\theta - \theta'))}{[2R(t)^2(1 - \cos(\theta - \theta')) + d(t)^2 + 2\sigma^2]^{3/2}}. \tag{B.6}$$

Hence, the evolution equation of the vortex ring radius, $R(t)$ reduces to:

$$\dot{R}(t) = v_r^{1,m} = \frac{\Gamma d(t)}{2\pi R(t)^2}\Psi[(d(t)^2 + 2\sigma^2)/(2R(t)^2)], \tag{B.7}$$

where Ψ is defined as:

$$\Psi(X^2) = \int_0^{2\pi} d\theta' \frac{\cos(\theta - \theta')}{[2(1 - \cos(\theta - \theta')) + 2X^2]^{3/2}}. \tag{B.8}$$

Similarly, the evolution equation of the spacing between the rings, $d(t)$, is given by:

$$\dot{d}(t) = v_z^{1,s} + v_z^{1,m} = \frac{\Gamma}{2\pi R(t)} \left(\Phi[(d(t)^2 + \sigma^2)/(2R(t)^2)] - \Phi[\sigma^2/R(t)^2] \right), \tag{B.9}$$

where Φ is defined as:

$$\Phi(X^2) = \int_0^{2\pi} d\theta' \frac{(1 - \cos(\theta - \theta'))}{[2(1 - \cos(\theta - \theta')) + 2X^2]^{3/2}}. \tag{B.10}$$

It is a simple matter to compute asymptotic expressions for the functions Φ and Ψ when $X^2 \to 0$ or $X^2 \to \infty$. To determine the evolution of $R(t)$ and $d(t)$, we numerically integrate Eq. (B.3), Eq. (B.7) and Eq. (B.9).

B.3.2   DYNAMIC EVOLUTION OF THE VORTEX RINGS

Eq. (B.3), Eq. (B.7), and Eq. (B.9) are used to compare the radial growth of the colliding vortex rings from the Biot-Savart model with the experimental data in the inset of Fig. 2.1(B) in the main text. This model agrees well with the mean radial growth of the rings prior to breaking down, at which point the assumptions of Biot-Savart are clearly violated. Here, we further compare the model against direct numerical simulations which describe the head-on collision of two vortex rings with the following initial conditions: $R(0) = R_0$, $d(0) = 2.5R_0$, and $\sigma(0) = 0.1R_0$. This choice of parameters allows for the direct comparison of the model with the DNS, starting from the same initial configuration. The DNS collision, where $Re_\Gamma = 4500$, was already presented in Fig. 2.2(B,D) of the main text and in Movie S3.
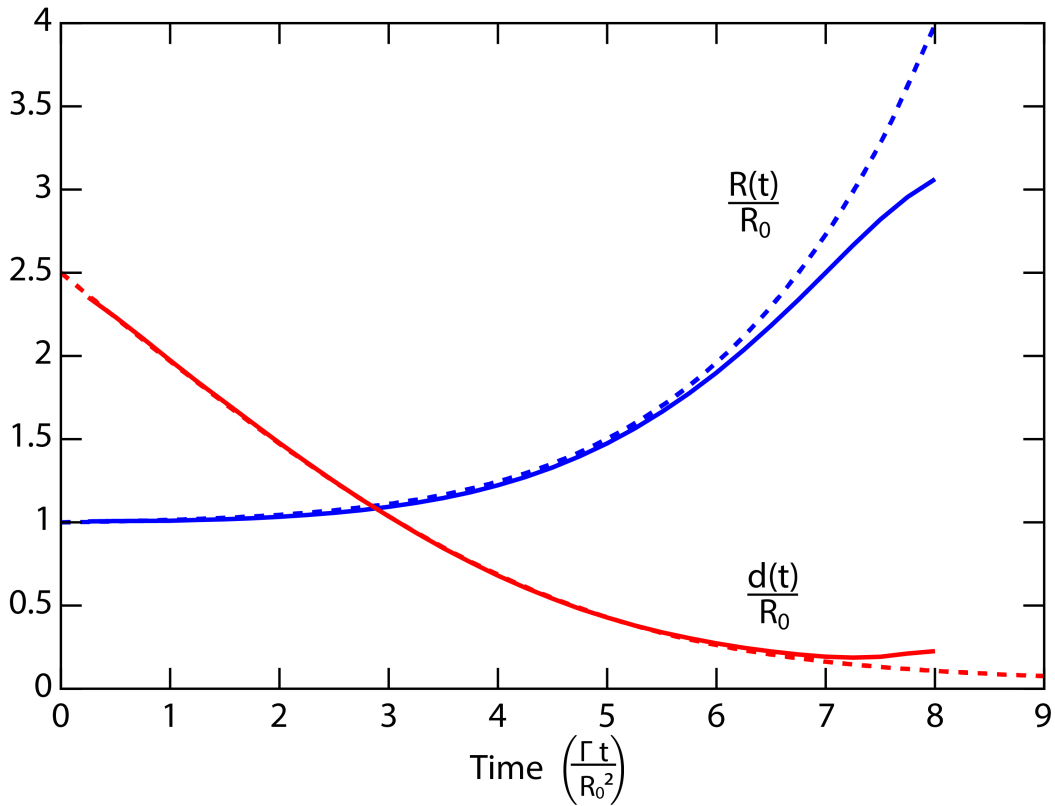
Figure B.3: Comparison between the evolution of the perpendicular spacing between the cores, $d(t)$, and the vortex ring radius, $R(t)$, obtained from DNS of the Navier-Stokes equations where $\mathrm{Re}_\Gamma = 4500$ (full lines) and from the Biot-Savart model (dashed lines). For both configurations, $d(0) = 2.5R_0$ and $\sigma(0) = 0.1R_0$.

Fig. B.3 shows the evolution of the vortex ring radius, $R(t)$, (blue curves) and the perpendicular distance between the filaments, $d(t)$, (red curves). The solution of the Biot-Savart model is shown with dashed lines, and the full lines correspond to the same configuration evaluated numerically by solving the Navier-Stokes equations. As the two rings initially approach one another, the distance between them decreases linearly. However, in both the Biot-Savart model and the DNS, the rings reach a minimum distance on the order of the core size before breaking down. During the late stage of the collision, the rings grow radially outwards; however, the growth of the ring radius predicted by the Biot-Savart model significantly exceeds that of the collision obtained from the DNS because

the core dynamics–and hence the breakdown–is not captured by Biot-Savart model.

B.3.3   Elliptical instability

Here we examine the the onset of the elliptical instability when the vortex rings collide head-on. We are primarily interested in the growth of short-wavelength modes, characteristic of the elliptical instability [40,39]. For this reason, we neglect the curvature of the rings and approximate the filaments with a pair of straight antiparallel vortices, located at $z = \pm d(t)/2$, with circulations $\pm\Gamma$, and each with a core radius $\sigma(t)$. The values of $d(t)$ and $\sigma(t)$ are determined from the solutions of the Biot-Savart model.

The onset of the elliptical instability results in the development of perturbations with a wavelength on the order of the core size [39]. Our analysis is based on the work of LeDizes, who examined the elliptical instability in the same flow configuration [37,38]. LeDizes derived the following equation for the growth rate, γ, of an infinitesimal perturbation of the vortex cores with a longitudinal wavenumber k_z:

$$\gamma = \frac{\Gamma}{8\pi d^2} \sqrt{\left(\frac{3}{4}\right)^4 K_{NL}(0)^2 - \frac{64d^4}{\sigma^4}\left(\frac{1}{2} - \cos(\zeta^{(m)})\right)^2 - \frac{8\pi k_z^2 d^2}{\mathrm{Re}_\Gamma \cos(\zeta^{(m)})}}, \qquad \text{(B.11)}$$

where $K_{NL}(0) = 1.5 + 0.038 \times 0.16^{-9/5} \approx 2.52$, and $\cos(\zeta^{(m)}) = \left(\frac{1}{2} - \frac{(2.26+1.69m)-k_z\sigma}{14.8+9m}\right)$.

In the expression for $\cos(\zeta^{(m)})$, m is an integer that distinguishes between several branches of solutions. We only examine the most unstable branch, corresponding to $m = 0$. To estimate the growth rate of the elliptical instability, we consider an azimuthal perturbation mode, n, along the rings. This corresponds to a wavenumber $q_n(t) = n/R(t)$. The growth of the radius, $R(t)$, implies that the wavenumber $q_n(t)$ decreases as time progresses for a fixed value of n. Note that when neglecting the curvature of the colliding rings, $k_z = q_n(t)$.

We evaluate the growth rate of the elliptical instability, $\gamma_n^{(m=0)}$, as a function of time for $n =$

120, 180, and 240, focusing on only the times when the growth rate is positive, as shown in Fig. B.4. These values of n were selected because they correspond to wavelengths that are on the order of the core radius, $\sigma(t)$, when the instability begins. We examine how the growth rates of these modes evolve when $\text{Re}_\Gamma = 3500$ (dotted-dashed lines), $\text{Re}_\Gamma = 4500$ (dashed lines) and $\text{Re}_\Gamma = 5000$ (full lines). The elliptical instability develops at each value of n only over a short period of time. The magnitude of the growth rate $\gamma_n^{(m=0)}$ increases as the Reynolds number increases.
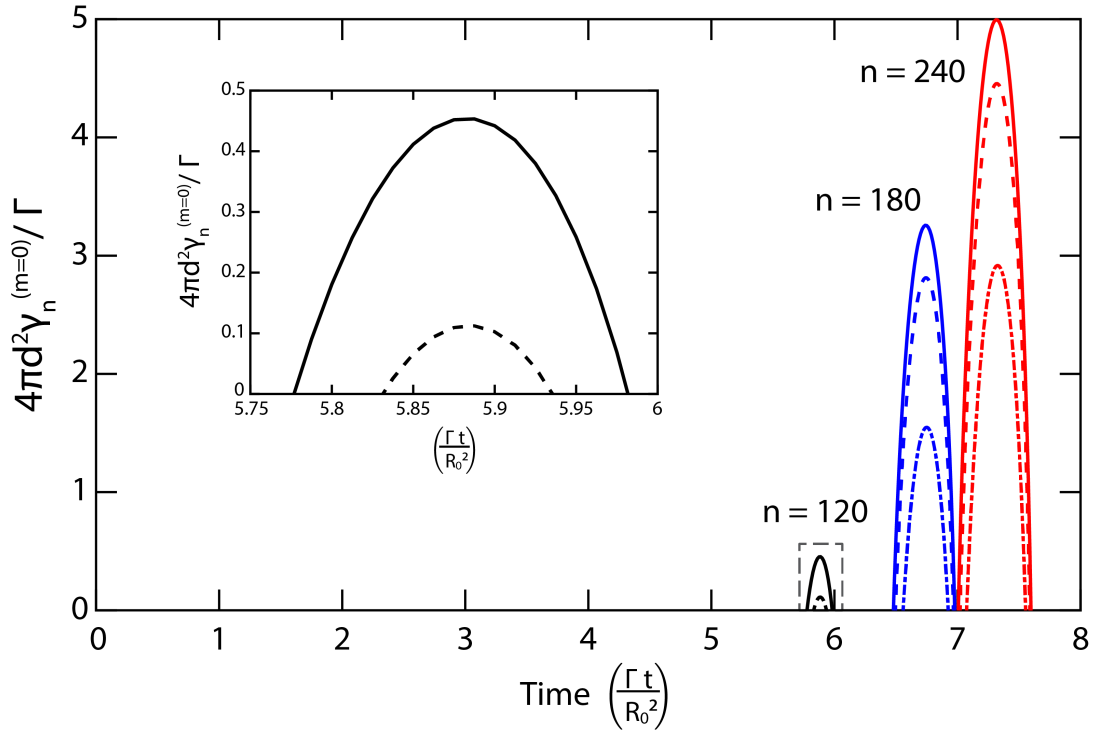
Figure B.4: Onset of the elliptical instability for colliding vortex rings. The normalized growth rate, γ_n, of three azimuthal perturbation modes, n, is evaluated for the head-on collision of two vortex rings using Eq. (B.11). (inset) zoomed-in view of the plot of the $n = 120$ mode indicated by the dashed gray box. The full lines, dashed lines, and dot-dashed lines correspond to $\text{Re}_\Gamma = 5000, 4500$, and 3500, respectively. The values of $R(t)$ and $d(t)$ are calculated from the Biot-Savart model, shown by the dashed lines in Fig. B.3 above.

The Biot-Savart model–Eq. (B.3), Eq. (B.7), and Eq. (B.9)–provides a semi-quantitative description of the solutions of the Navier-Stokes equations when the $n = 120$ mode becomes un-

stable, as shown in the inset of Fig. B.4. At this time, $\Gamma t / R_0^2 = 5.9$, the unstable wavelength is $\lambda \approx 2\pi R(t)/120 \approx 2\sigma(t)$. The model therefore predicts that perturbations with a wavelength on the order of the core size are unstable due to the elliptical instability mechanism when $\mathrm{Re}_\Gamma = 4500$, but are stable for $\mathrm{Re}_\Gamma = 3500$, in qualitative agreement with our findings. The elliptical instability is still triggered for the $\mathrm{Re}_\Gamma = 3500$ configuration, albeit at later times. The model also demonstrates that the onset of the elliptical instability for $\mathrm{Re}_\Gamma = 4500$ occurs when the spacing between the rings, $d(t)$, reaches the minimum threshold on the order of the initial core thickness, $2\sigma_0 = 0.2R_0$, as shown in Fig. B.3. This is consistent with the experimental and DNS results shown in Fig. 2.2(C-D) in the main text.

B.4   Nonlinear development of the elliptical instability

B.4.1   Formation of secondary vortex filaments

Following the development of antisymmetric perturbations that result from the elliptical instability, an array of secondary vortex filaments spontaneously forms perpendicular to the original vortex cores. This has been directly observed experimentally and numerically for vortex ring collisions, as detailed in the main text. The same flow structures emerge via the elliptical instability during the interaction between two antiparallel vortex tubes[40,35]. This observation seems at first surprising, as it indicates the emergence of a component of circulation in the plane separating the two vortices, where the vorticity is initially zero. If the midplane separating the two vortices (i.e. the $z = 0$ plane) were a plane of symmetry–as is the case in many studies examining the Crow instability[10] of interacting vortex tubes[60,26]–the vorticity along this plane would remain zero at all times. The antisymmetric nature of the perturbed vortex cores, shown in Fig. 2.2(A-B) of the main text, however, allows for the development of a non-zero circulation in the collision plane. Here, we examine how a significant component of the circulation can accumulate on the plane $z = 0$, referred to here as the

plane of reflection, as shown in Fig. 2.4(C-D) in the main text.

We examine the same direct numerical simulation presented in Fig. 2.4 in the main text and Movie S5, consisting of two, initially parallel, counter-rotating vortex tubes with $\text{Re}_\Gamma = 4500$. We examine the evolution of the normal vorticity component, ω_x, along a fixed axial cross-section of the tubes, as shown in Fig. B.5. The upper vortex rotates in the clockwise direction, and the lower
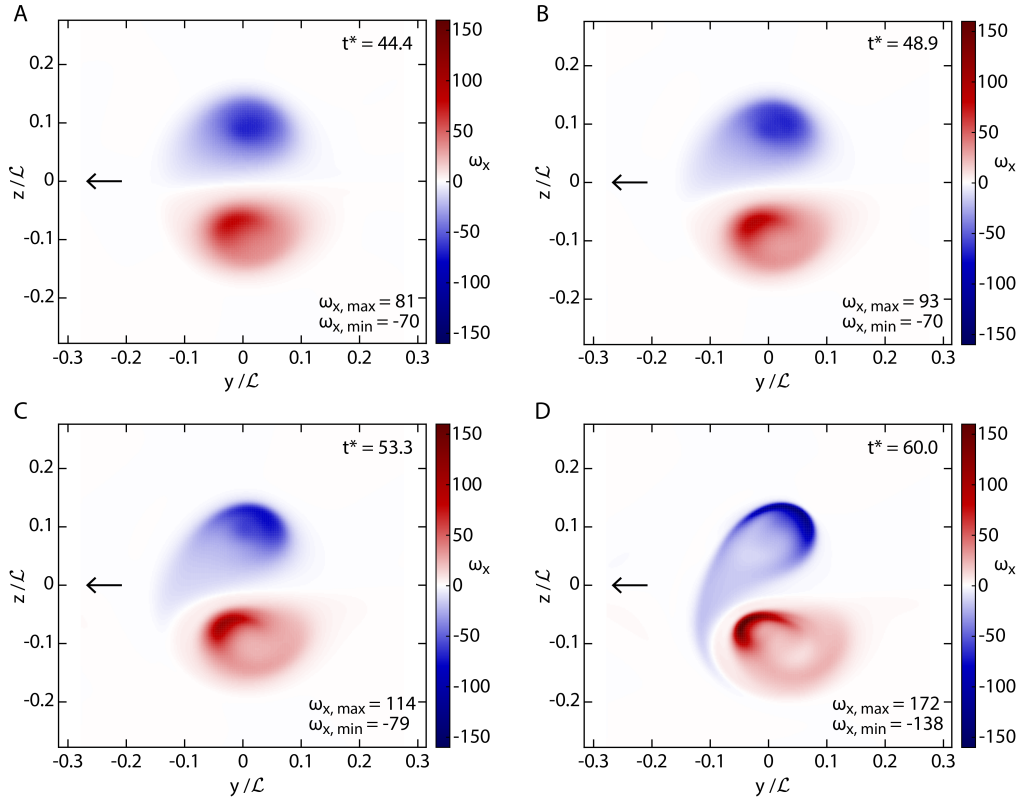
Figure B.5: Formation of a secondary vortex filament. Temporal evolution of the axial vorticity distribution, $\omega_x(y, z)$, along a fixed cross section at $x/\mathcal{L} = 0.48$ for DNS of counter-rotating vortex tubes where $\text{Re}_\Gamma = 4500$. The black arrows indicate the propagation direction, though a horizontal offset is applied at each time to keep the vortices in the center of the domain. (A) The vorticity from the two vortex tubes is initially separated along the ($z = 0$) reflection plane. (B) As the perturbations develop, the lower core migrates to the leading direction and the upper core migrates to the trailing end. (C) The cores flatten into sheet-like structures, and vorticity from the upper vortex is advected down to the lower vortex. (D) The cores contract into highly curved, sheetlike structures where the vorticity is concentrated. The advected vorticity forms a secondary vortex filament across the ($z = 0$) reflection plane. Note: $\sigma = 0.06\mathcal{L}$, $b = 2.5\sigma$, and $t^* = \Gamma t/b^2$.

vortex rotates in the opposite direction, resulting in their propagation in the negative $y-$direction, indicated by the black arrows. Initially, the vorticity of the tubes largely remains on the respective sides of the plane of reflection, as shown in Fig. B.5(A). However, once the tubes become perturbed, the centroids of the vortex cores deform such that the lower core moves forward in the propagation direction and the upper core moves backward, as shown in Fig. B.5(B-D). This contrary motion of the cores illustrates the antisymmetric structure of the perturbations, as this particular cross section is located along an anti-node of the pair. While the amplitudes of the perturbations grow, the vorticity distributions of the cores contract and amplify into flattened, sheet-like structures, as shown in Fig. B.5(D) and Fig. 2.4(A) in the main text. The curvatures of the deformed cores are of opposite sign; the leading vortex core is curved toward the propagation direction and vice-versa for the trailing core. Additionally, the lower core, which is deflected toward the leading edge of the vortex pair, has a higher curvature than that of the upper core. The tendency of the kinked, perturbed cores to locally flatten into vortex sheets results from the stretching field generated by each filament, as characterized by the Biot-Savart model. An elementary calculation predicts that, on the outer side of a kinked filament, the vorticity is stretched and grows, while on the inner side, the vorticity decreases (see Fig. 4 of[60]). The tendency of the perturbed vortex cores to flatten into sheets is therefore the result of the dynamics of kinked vortex tubes.

Because the perturbations of the vortex cores are periodic, the relative positions of the cores revert every half-wavelength along the axial direction of the tubes, as shown in Fig. B.6. The 3D visualization of the vorticity modulus, $|\omega|$, shows how the peaks of the perturbed cores flatten into mushroom-cap structures, as shown in Fig. B.6(A). By lowering the threshold of the vorticity modulus, as shown in Fig. B.6(B), one can visualize how the edges of the flattened cores roll up into two secondary vortex filaments that are pulled toward the opposite vortex tube. Moving along the axial direction, the leading vortex switches from the top core (Fig. B.6(C)) to the bottom core (Fig. B.6(E)). At the nodes of the perturbations, the cores are aligned with each other, as shown in
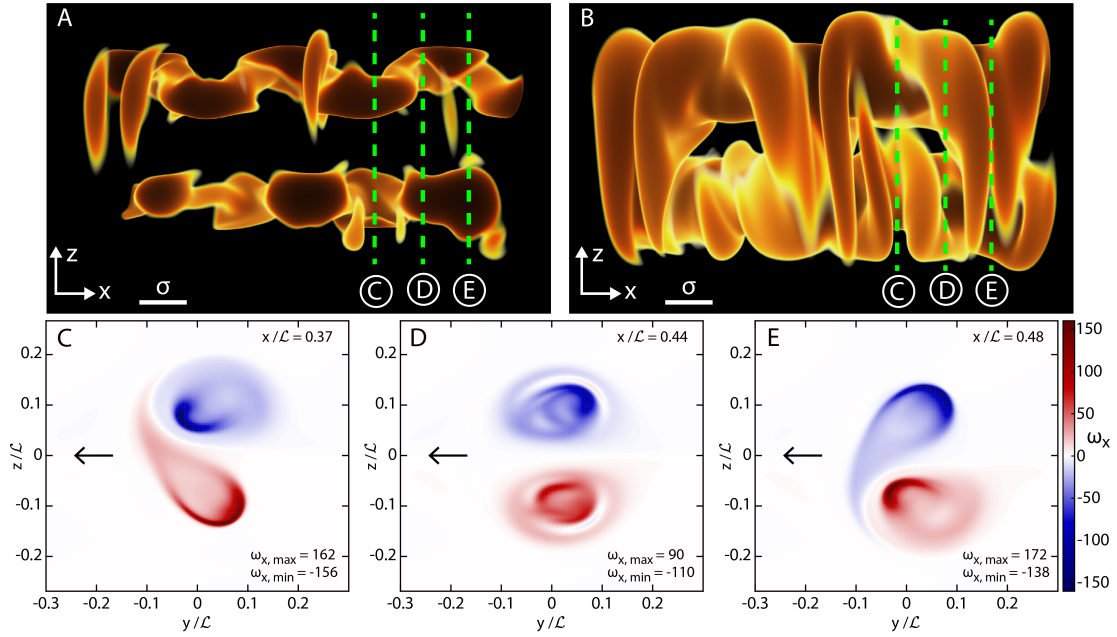
Figure B.6: Alternating structure of secondary filaments. DNS of counter-rotating vortex tubes where Re_Γ=4500 at a fixed time, $t^* = \Gamma t/b^2 = 60.0$. (A-B) 3D vorticity modulus of the simulated flow and (C-E) distribution of axial vorticity, $\omega_x(y,z)$, along cross sections of the tubes indicated by the dashed green lines. The black arrows indicate the propagation direction of the vortex pair. (A) The cores flatten into vortex sheets at the tips of each perturbation ($0.092 \leq |\omega|/|\omega|_{\mathrm{max}} \leq 0.122$). (B) The edges of the each flattened perturbation roll up into pairs of secondary filaments ($0.031 \leq |\omega|/|\omega|_{\mathrm{max}} \leq 0.053$). Due to the antisymmetric structure of the perturbations, the orientation of the secondary filament pairs alternates periodically. (C) At anti-nodes where the top vortex core leads, the secondary filament is stretched up from the lower vortex tube. (D) At nodes, neither vortex core leads and no secondary filaments form. (E) At anti-nodes where the bottom vortex core leads, the secondary filament is stretched down from the upper vortex tube. Note: $\sigma = 0.06\mathcal{L}$ and and $b = 2.5\sigma$.

Fig. B.6(D). Notably, the inherent asymmetry of the offset vortices causes the highly curved, leading core to locally advect the low-vorticity region of the trailing core around itself, as previously shown in Fig. B.5. This shedding of vorticity repeats along each anti-note peak of the perturbed cores, leading to an alternating array of perpendicular secondary filaments that traverse the plane of reflection, as shown in Fig. B.6(B). The alternation of pairs of secondary filaments accounts for the interdigitation of the colliding vortices visualized with dye both experimentally and numerically in the main text. The counter-rotating structure of adjacent secondary filaments, as shown in Fig. 2.4(D) in the

main text, results from two sources. First, the edges of each flattened perturbation roll up into a pair of secondary filaments that counter-rotate relative to one another. Additionally, the alternating orientation of the secondary vortex pairs cause filaments formed from adjacent perturbations to counter-rotate with each other.

B.4.2 Transfer of circulation

The dynamics of the thin secondary filaments, transported across the reflection plane ($z = 0$), vary along the axial direction. This implies that the axial component of the circulation in the half-plane,

$$\Gamma_x(x,t)\Big|_{z\to-\infty}^{z=0} \equiv \int_{-\infty}^{\infty} dy \int_{-\infty}^{0} dz\, \omega_x(x,y,z,t) \tag{B.12}$$

varies, both as a function of time and of x. By integrating the vorticity distribution on the lower half plane at several times, we find that the axial component of circulation varies periodically with x, as shown in Fig. B.7(A). This demonstrates how the formation and stretching of the secondary filaments develop a periodic transfer of vorticity from the original tubes through the reflection plane. Once the secondary filaments are fully formed after $t^* \gtrsim 65$, however, the variations in the axial component of circulation saturate.

Concomitantly, as the axial component of circulation is drained from the lower vortex tube, the secondary filaments traverse through the reflection plane, $z = 0$. The corresponding flux of vorticity in the transverse direction is quantified by computing the transverse component of circulation $\Gamma_z(x,t)$ along the reflection plane on $[0,x]$:

$$\Gamma_z(x,t) \equiv \int_{0}^{x} dx' \int_{-\infty}^{+\infty} dy'\, \omega_z(x',y',z=0) \tag{B.13}$$

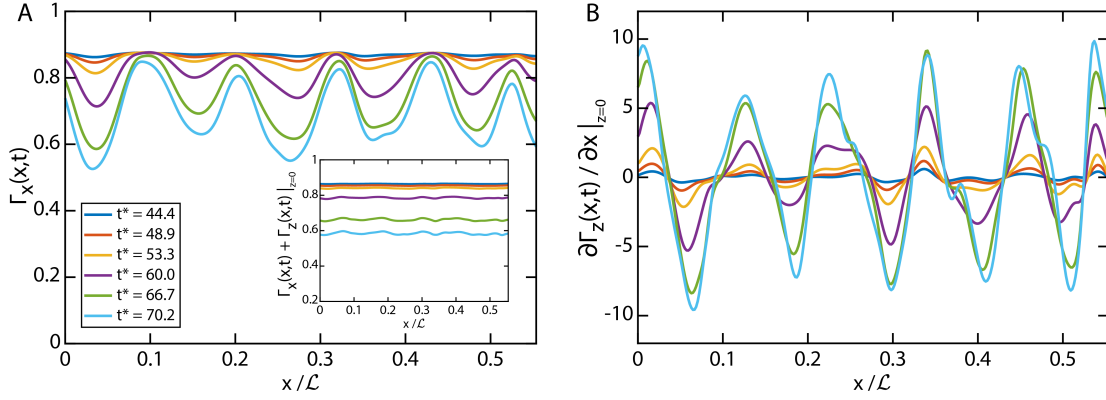The derivative of $\Gamma_z(x,t)$ with respect to x reduces Eq. (B.13) into the normalized sum of the

Figure B.7: Evolution of circulation. DNS of counter-rotating vortex tubes where $Re_\Gamma = 4500$. (A) Evolution of the axial component of circulation, $\Gamma_x(x,t)$, in the lower half plane (y,z) for $z < 0$. (inset) Evolution of the axial and transverse components of circulation, $\Gamma_x(x,t) + \Gamma_z(x,t)$. (B) Evolution of the derivative of the transverse component of circulation, $\partial\Gamma_z/\partial x$ along the reflection plane $(z = 0)$.

transverse vorticity, ω_z, along a line located at the axial position, x, on the reflection plane, as shown in Fig. B.7(B) at various times. The sinusoidal nature of $\partial\Gamma_z(x,t)/\partial x|_{z=0}$–about a mean value of zero–along the axial direction showcases the counter-rotating structure of adjacent secondary filaments, as shown in Fig. 2.4(D) in the main text.

An important relation between $\Gamma_z(x,t)$ and $\Gamma_x(x,t)$ results from the observation that $\nabla \cdot \boldsymbol{\omega} = 0$; that is, the flux of vorticity a through a closed surface limiting a finite volume of fluid is conserved. We define the half-plane $\mathcal{P}_\alpha$ by the conditions $x = \alpha$ and $z \leq \alpha$, and the band $\mathcal{Q}_{\alpha\beta}$ for $\alpha \leq \beta$ by $z = 0$ and $\alpha \leq x \leq \beta$. Additionally, we use the property that $\nabla \cdot \boldsymbol{\omega} = 0$ to the domain limited by $\mathcal{P}_\alpha$, $\mathcal{Q}_{\alpha\beta}$, and $\mathcal{P}_\beta$, with $\alpha \leq \beta$. An elementary calculation shows that the flux of $\boldsymbol{\omega}$ on this domain reduces to $\big(\Gamma_x(\beta,t) + \Gamma_z(\beta,t)\big) - \big(\Gamma_x(\alpha,t) + \Gamma_z(\alpha,t)\big)$. Thus, the condition that the flux of vorticity is zero imposes that $\Gamma_x(x,t) + \Gamma_z(x,t)$ does not dependent on x. We find that our numerical results satisfy this conservation relation, as shown in the inset of Fig. B.7.

Physically, the relation $\partial_x\big(\Gamma_x(x,t) + \Gamma_z(x,t)\big) = 0$ imposes that the axial variations of $\Gamma_x(x,t)$, clearly visible in Fig. B.7(A), necessitate the variations of the flux $\Gamma_z(x,t)$, which are proportional to the transverse circulation in the plane $z = 0$. That is, because the circulation of the system is

conserved–aside from viscous dissipation–any axial circulation lost from the vortex tubes is redirected to the secondary filaments through the transfer of transverse circulation. The fluctuations of $\Gamma_x(x, t)$ correspond to $\approx 0.25\Gamma_0$, implying that in the configuration studied here, the circulation of each transverse secondary filament is approximately $1/4$ of the axial component of circulation in the original tubes.

B.5 INTERACTIONS OF SECONDARY VORTEX FILAMENTS

Through the creation of secondary filaments, the elliptical instability provides a mechanism by which smaller generations of counter-rotating vortex filaments form and interact to generate small-scale flow structures. During the evolution of the elliptical instability, the development of antisymmetric perturbations in the cores leads to the formation of an array of counter-rotating secondary filaments, as shown numerically for a typical example in Fig. B.8(A), Movie S6, and Movie S7, where $\mathrm{Re}_\Gamma = 3500$. Neighboring secondary filaments interact with one another in the same manner as the initial vortex tubes. Because the secondary filaments are smaller and have a lower circulation than the original vortex tubes, they can be viewed as having a lower effective Reynolds number. These adjacent secondary filaments align with one another in pairs, as shown in Fig. B.8(B-C). Due to their counter-rotation, the filaments exert large strains on each other, which causes one of the secondary filaments to flatten into a vortex sheet, as shown in Fig. B.8(D). Upon further stretching, this vortex sheet splits into two smaller tertiary vortex filaments, as shown in Fig. B.8(E-F). This breakdown mechanism in which counter-rotating vortex filaments interact, flatten into vortex sheets, and split into even smaller generations of vortices has been previously observed in vortex ring collisions[45] and is attributed to the late-stage development of the Crow instability[10]. This instability dominates during the interaction of vortices at low-Reynolds numbers, like that of the secondary vortex filament pair.
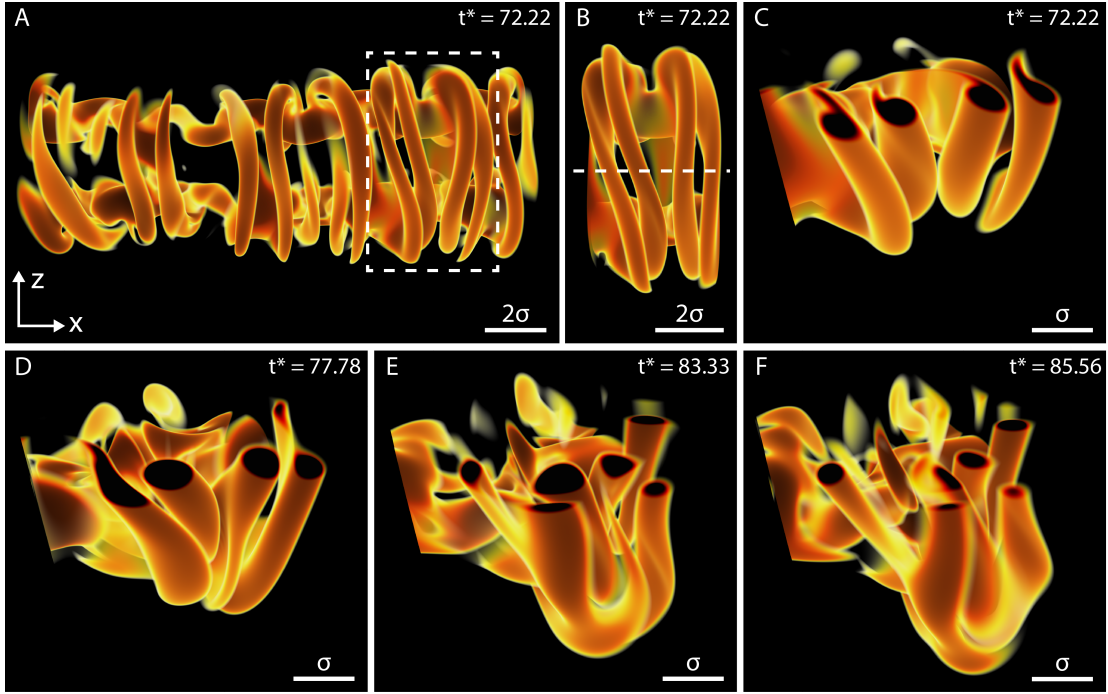
Figure B.8: Interactions of secondary vortex filaments. Vorticity modulus of a simulated vortex tube interaction where $Re_\Gamma = 3500$. (A) Array of secondary filaments formed during the late-stage evolution of the elliptical instability. (B) Zoom-in view of two pairs of secondary filaments indicated by the dashed box. (C) Cross-sectional view of the secondary filaments through the plane of reflection $(z = 0)$, indicated by the dashed line in (B). Neighboring filaments counter-rotate and interact with each other. (D) Interacting secondary filaments deform from the mutual strain and one of the filaments locally flattens into a vortex sheet. (E) The flattened vortex sheet splits into two smaller tertiary vortex filaments. (F) The newly-formed tertiary filaments unravel the secondary filament. For (A-F), the vorticty threshold is $0.122 \leq |\omega|/|\omega|_{max} \leq 0.206$, where $|\omega|_{max}$ is the maximum vorticity modulus for the entire simulation. Note: $\sigma = 0.06\mathcal{L}$, $b = 2.5\sigma$, and $t^* = \Gamma t/b^2$.

As shown previously, only a fraction of the initial circulation is transferred to the secondary filaments. Even though the elliptical instability fully develops during the $\text{Re}_\Gamma = 3500$ configuration, the effective Reynolds number of the interacting secondary filaments is not sufficient enough for the elliptical instability to develop again. Instead, the Crow instability dominates during this second iteration, and the secondary vortices flatten into vortex sheets and split into smaller tertiary filaments. In order for the secondary filaments to, themselves, interact through the elliptical instability and form a tertiary generation of perpendicular filaments–as shown in Fig. 2.5 in the main text and in Movie S9–the initial counter-rotating vortex tubes must have a higher Reynolds number.

B.6   Analysis of the transfer of energy in a turbulent flow

This section examines the derivation and meaning of the shell-to-shell energy transfer spectrum, $T(k,t)$, introduced in the main text and plotted in Fig. 2.5(G). A typical method for characterizing a turbulent flow, which encompasses of a wide range of excited scales of motion, is to examine evolution of the the energy spectra in Fourier space. This energy spectrum is designated by the term $E(k,t)$, such that $E(k,t)\,dk$ is the amount of kinetic energy at time t, in a shell in wavenumber space between k and $k + dk$. In the absence of forcing, and in the simplified case of a homogeneous isotropic flow, one can derive from the Navier-Stokes equations the following energy balance [57,42]:

$$\frac{\partial E(k,t)}{\partial t} + T(k,t) = -2\nu k^2 E(k,t). \tag{B.14}$$

The terms in this equation state that for a given wavenumber, k, and at any time, t, the rate of change of the energy of that mode plus the rate of energy transferred to or from that wavenumber via other modes is balanced by the viscous dissipation of that mode. In this equation, $T(k,t)$ origi-

nates from the nonlinear, advective term in the Navier-Stokes equations:

$$T(k,t)\,dk = \sum_{k \leq |\mathbf{k}| \leq k+dk} \Re\big(\overline{(\mathbf{u} \cdot \nabla)\mathbf{u}}(\mathbf{k}) \cdot \overline{\mathbf{u}}(-\mathbf{k})\big). \tag{B.15}$$

While Eq. (B.14) is often used in a context of fluid turbulence, it can be applied to any solution of the Navier-Stokes equations. In our direct numerical simulations, $T(k,t)$ is calculated by applying a discrete Fourier transform to both our solved flow field, $\mathbf{u}(\mathbf{x},t)$ and the nonlinear term, $(\mathbf{u} \cdot \nabla)\mathbf{u}(\mathbf{x},t)$, which are then applied to Eq. (B.15).

B.7   Emergence of turbulence from the elliptical instability with increasing Reynolds number

B.7.1   Dissipation rate evolution and energy spectra

Direct numerical simulations of the interacting, counter-rotating vortex tubes are performed at a range of Reynolds numbers to examine by what mechanism the onset of the elliptical instability leads to the development of turbulence. At each Reynolds number, the energy dissipation rate, ε, qualitatively follows the same temporal evolution, as shown in Fig. B.9(A). The coherent vortex tubes initially interact, and the rapid increase in ε is initiated by the onset of the elliptical instability at each Reynolds number, as shown in Fig. 2.5 in the main text. The dissipation rate is maximized during the late-stage of the elliptical instability, in which the secondary filaments interact with each other and the remnants of the original primary vortex cores. As the Reynolds number is increased, the maximum dissipation rate increases. Because the viscous dissipation of energy in the flow primarily occurs on the smallest scales of the system, this behavior indicates that the high-Reynolds number configurations more effectively convey energy into small-scale flow structures.

Additionally, we examine the normalized kinetic energy spectra, $E(k)/(\eta^{\frac{1}{4}}\nu^{\frac{5}{4}})$, when the dissi-
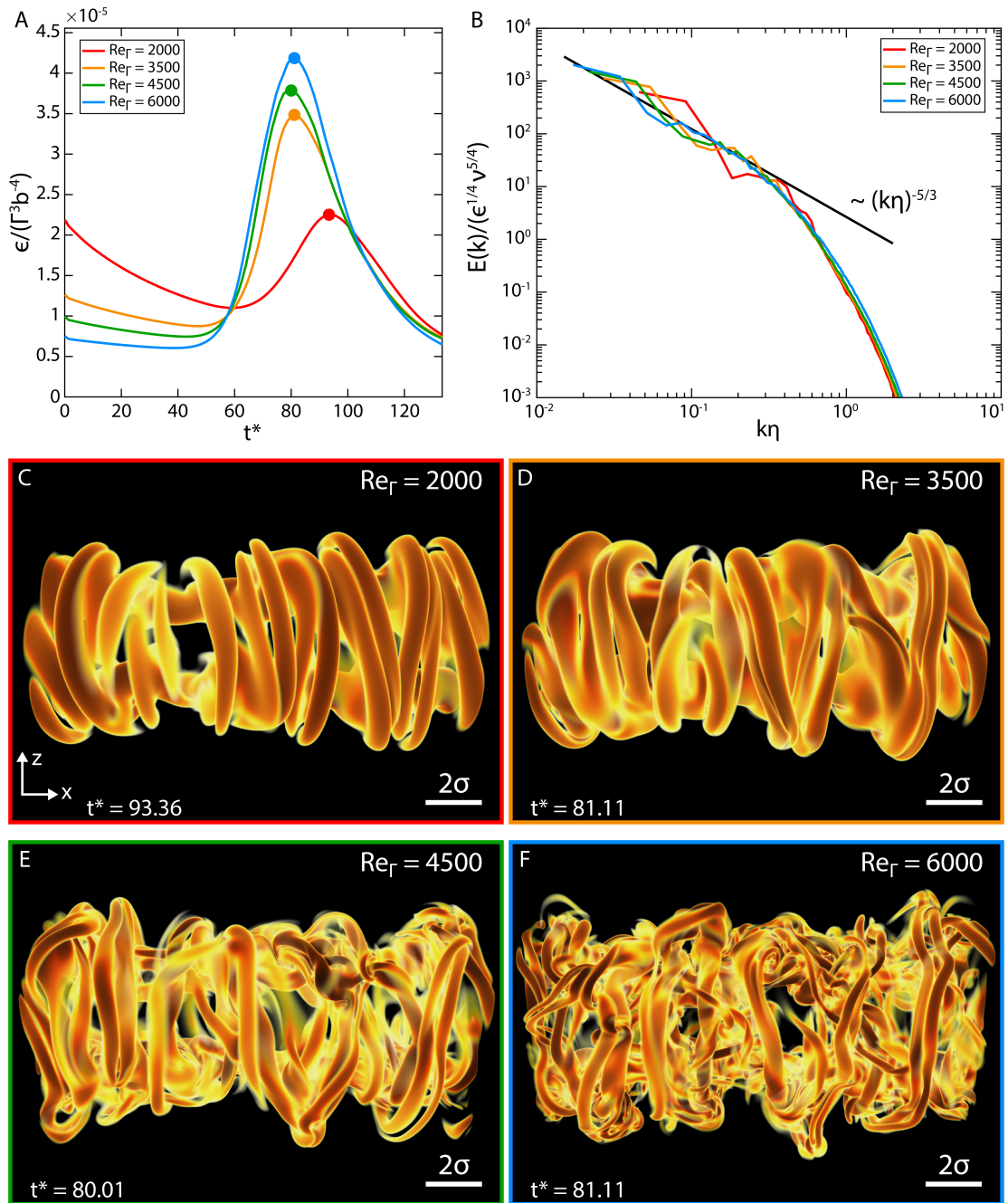
Figure B.9: Dissipation rate evolution and energy spectra for simulated vortex tube interactions at various Reynolds numbers. (A) Evolution of normalized kinetic energy dissipation rate. The markers indicate the maximum energy dissipation rate. (B) Normalized kinetic energy spectra at the peak dissipation rate, where the black line corresponds to Kolmogorov scaling. (C-F) Snapshots of the 3D vorticity modulus at the times corresponding to the maximum dissipation rate for each Reynolds number. The vorticity thresholds are $0.153 \leq |\omega|/|\omega|_{max} \leq 0.305$ for (C) and $0.061 \leq |\omega|/|\omega|_{max} \leq 0.183$ for (D-F). For each simulation, $\sigma = 0.06\mathcal{L}$, $b = 2.5\sigma$, $\text{Re}_\Gamma = \Gamma/\nu$, and $t^* = \Gamma t/b^2$.

pation rate is maximized for each Reynolds number, as shown in Fig. B.9(B). Each of the energy spectra generally follow the $\sim (k\eta)^{-5/3}$ Kolmogorov scaling of turbulence, where η is the dissipative length scale[34]. Notably, the agreement of the simulated energy spectra with this turbulent scaling improves for simulations that are carried out at higher Reynolds numbers. This is because the inertial range of the breakdown is more developed at higher Reynolds numbers–i.e. there is a larger range of scales over which Kolmogorov's axioms for turbulence are valid[34]. The emergence of this multi-scale turbulent behavior is encapsulated by the snapshots in Fig. B.9(C-F) which show the vorticity modulus of the interacting tubes at each Reynolds number when ε is maximized.

In each configuration, the elliptical instability is fully developed at the peak dissipation rate, as an array of perpendicular secondary filaments bridges the gap between the original vortex tubes. These stretched, counter-rotating secondary filaments interact with each other and the remnants of the original tubes through different means at each Reynolds number. For the $Re_\Gamma = 2000$ configuration, the secondary filaments do not have sufficient circulation to interact with one another and break down further, as viscous dissipation sets in (see Movie S11[48]). When the Reynolds number is raised to 3500, neighboring secondary filaments locally interact with one another, flatten into vortex sheets, and split into smaller tertiary filaments, as shown in Movie S6 and Movie S7[48]. The same interactions between secondary filaments occur for the $Re_\Gamma = 4500$ configuration; however, the secondary filaments become more disordered as they undergo complex 3D motion and become wrapped around each other and the original tubes, breaking down into fine-scale vortex filaments (see Movie S5[48]). Lastly, in the $Re_\Gamma = 6000$ configuration, the secondary filaments rapidly emerge, interact, and violently break down as they almost instantaneously burst into an ensemble of vortices interacting over a wide range of scales, as shown in Movie S8[48]. Notably, the high-circulation secondary filaments in this configuration locally interact to form new generations of perpendicular tertiary filaments, as shown in Fig. 2.5 in the main text and in Movie S9[48]. We propose that these tertiary filaments form through another iteration of the elliptical instability.

These results demonstrate how the elliptical instability provides a mechanism by which counter-rotating vortex tubes at high Reynolds numbers interact and break down to develop a turbulent cascade. This iterative instability generates new vortices that interact with each other and "grind down" into smaller and smaller vortex filaments before being dissipated through viscosity[76].

B.7.2 Vorticity evolution

The evolution of the vorticity modulus in the simulated vortex tube interactions also indicates the onset of a turbulent state during the breakdown of the tubes, which is especially pronounced for high-Reynolds number configurations. For each Reynolds number, the maximum vorticity modulus, $|\omega|_{\max}$, remains initially constant until it increases during onset of the elliptical instability, as shown in Fig. B.10(A). For the $\mathrm{Re}_\Gamma = 2000$ configuration, the maximum vorticity modulus increases slightly during the formation and stretching of the secondary filaments; however, because the filaments do not interact due to the onset of viscous dissipation, the maximum vorticity modulus decreases. For the higher-Reynolds number configurations, the maximum vorticity modulus increases precipitously due to the formation and stretching of the secondary filaments and remains sustained at a heightened level before decreasing due to viscous dissipation. This heightened level of $|\omega|_{\max}$ coincides with the maximization of the energy dissipation rate, ε, as shown in Fig. B.9(A). The sustained amplification of the maximum vorticity modulus thus results from the new generation and local interactions of small-scale vortices during the turbulent breakdown. The higher the Reynolds number, the longer the maximum vorticity modulus remains at this elevated level before viscosity damps out the motion of the vortices.

Additionally, the mean vorticity modulus, $\overline{|\omega|}$, increases during the onset of the elliptical instability, reaches a peak value approximately when the dissipation rate, ε, is maximized, and decreases as viscosity damps out the small-scale motion of the flow, as shown in Fig. B.10(B). The increase in the mean vorticity modulus indicates how the initially localized and coherent flow becomes more
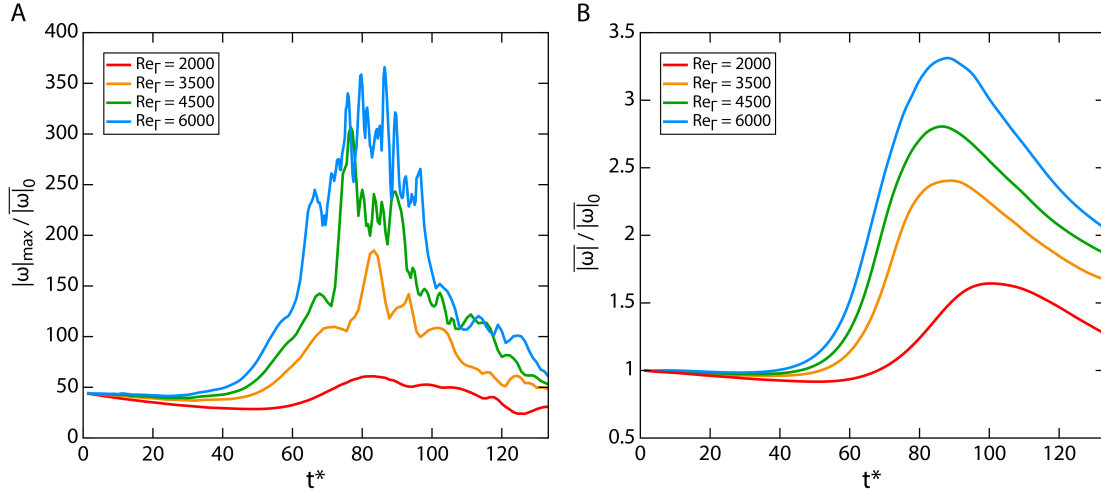
Figure B.10: Vorticity evolution for simulated vortex tube interactions at various Reynolds numbers. (A) Maximum vorticity modulus and (B) mean vorticity modulus evolution. Both moduli are normalized by the initial mean vorticity modulus. For each simulation, $\sigma = 0.06\mathcal{L}$, $b = 2.5\sigma$, $\mathrm{Re}_\Gamma = \Gamma/\nu$, and $t^* = \Gamma t/b^2$.

distributed throughout the domain during the breakdown. The amplification of the mean vorticity with increasing Reynolds number further demonstrates how the turbulent breakdown in the high-Reynolds number configurations is more three-dimensional and quasi-isotropic.

B.8 Supplemental movie descriptions

Movie S1. Head-on collision of vortex rings.

Underwater view of the head-on collision of two vortex rings dyed separately, where $\mathrm{Re} = UD/\nu = 6000$ and $\mathrm{SR} = L/D = 2.5$. The rings expand radially as they collide at the midplane before rapidly breaking down into a turbulent cloud of dye.

Movie S2. Experimental vortex ring collision with dyed cores.

Head-on view (top) and side view (bottom) showing the core dynamics of two colliding vortex rings, where $\mathrm{Re} = 7000$ and $\mathrm{SR} = 2.0$. As the rings stretch radially during the collision, the cores develop antisymmetric, short wavelength perturbations, indicative of the elliptical instability. Once

fully formed, the perturbations deflect out-of-plane and break down into a turbulent cloud of dye.

Movie S3. DNS of dyed vortex ring collision.

Overhead view (top) and side view (bottom) showing the simulated collision of two vortex rings dyed red and blue, respectively ($\text{Re}_\Gamma = \Gamma/\nu = 4500$ and $t^* = \Gamma t/R_0^2$). The dye in the cores of the rings (dark) is differentiated from the dye surrounding the cores (light). As the rings collide, they stretch radially and develop antisymmetric, short-wavelength perturbations, indicative of the elliptical instability. As a result of these perturbations, the vortex rings interdigitate, forming alternating pairs of secondary vortex filaments, perpendicular to the cores. The rings then rapidly break down into a turbulent cloud of dye.

Movie S4. Experimental fully dyed vortex ring collision.

Overhead view (top) and side view (bottom) showing the collision of two vortex rings, where Re = 6000 and SR = 2.5. As the vortex rings collide, they develop alternating "tongues" that interdigitate around one another. The edges of these tongues roll up into an ordered array of secondary vortex filaments, perpendicular to the vortex cores. These secondary filaments interact and rapidly break down into a turbulent cloud of dye.

Movie S5. DNS of vortex tube interaction: $\text{Re}_\Gamma = 4500$.

Vorticity modulus for the simulated interaction of two antiparallel vortex tubes, where $\text{Re}_\Gamma = 4500$ and $t^* = \Gamma t/b^2$. As a result of the elliptical instability, the cores develop antisymmetric perturbations, and an array of counter-rotating secondary vortex filaments forms perpendicular to the cores. The secondary filaments interact with each other and the remains of the cores before breaking down into a "soup" of small-scale vortices that are dissipated by viscosity. The vorticity threshold is $0.076 \leq |\omega|/|\omega|_{\max} \leq 0.198$, and the tubes propagate in the $-y$ direction.

Movie S6. DNS of vortex tube interaction: $\text{Re}_\Gamma = 3500$.

Vorticity modulus for the simulated interaction of two antiparallel vortex tubes, where $\mathrm{Re}_\Gamma = 3500$ and $t^* = \Gamma t/b^2$. As a result of the elliptical instability, the cores develop antisymmetric perturbations, and an array of counter-rotating secondary vortex filaments forms perpendicular to the cores. The secondary filaments interact with each other and the remains of the cores before breaking down into a "soup" of small-scale vortices that are dissipated by viscosity. The vorticity threshold is $0.122 \le |\omega|/|\omega|_{\mathrm{max}} \le 0.275$, and the tubes propagate in the $-y$ direction.

Movie S7. Interaction and splitting of secondary vortex filaments.

Vorticity modulus for the simulated interaction of two antiparallel vortex tubes, where $\mathrm{Re}_\Gamma = 3500$ and $t^* = \Gamma t/b^2$. Neighboring secondary filaments counter-rotate and interact with one another. This close-range interaction causes one of the filaments to become flattened into a vortex sheet before splitting into smaller tertiary vortex filaments. The vorticity threshold is $0.122 \le |\omega|/|\omega|_{\mathrm{max}} \le 0.206$.

Movie S8. DNS of vortex tube interaction: $\mathrm{Re}_\Gamma = 6000$.

Vorticity modulus for the simulated interaction of two antiparallel vortex tubes, where $\mathrm{Re}_\Gamma = 6000$ and $t^* = \Gamma t/b^2$. As a result of the elliptical instability, the cores develop antisymmetric perturbations, and an array of counter-rotating secondary vortex filaments forms perpendicular to the cores. The secondary filaments and remaining cores interact violently and rapidly "burst" into a turbulent flow of vortices interacting over many scales. Viscosity damps out the motion of the remaining vortices. The vorticity threshold is $0.077 \le |\omega|/|\omega|_{\mathrm{max}} \le 0.153$, and the tubes propagate in the $-y$ direction.

Movie S9. Iterative cascade of elliptical instabilities.

Vorticity modulus for the simulated interaction of two antiparallel vortex tubes, where $\mathrm{Re}_\Gamma = 6000$ and $t^* = \Gamma t/b^2$. Neighboring secondary filaments violently interact and form another gener-

ation of perpendicular, tertiary filaments through the elliptical instability. The vorticity threshold is $0.092 \leq |\omega|/|\omega|_{\max} \leq 0.214$.

Movie S10. Gaussian fit to vortex core PIV data.

2D PIV measurement of the vorticity distribution of a formed vortex ring, where $\mathrm{Re} = 7000$ and $\mathrm{SR} = 2.5$. The raw PIV vorticity data is plotted in the top panel and the Gaussian fit of the top and bottom cores is plotted in the bottom panel.

Movie S11. DNS of vortex tube interaction: $\mathrm{Re}_\Gamma = 2000$.

Vorticity modulus for the simulated interaction of two antiparallel vortex tubes, where $\mathrm{Re}_\Gamma = 2000$ and $t^* = \Gamma t/b^2$. As a result of the elliptical instability, the cores develop antisymmetric perturbations, and an array of counter-rotating secondary vortex filaments forms perpendicular to the cores. The secondary filaments have little circulation and quickly dissipate due to viscosity. The vorticity threshold is $0.229 \leq |\omega|/|\omega|_{\max} \leq 0.458$, and the tubes propagate in the $-y$ direction.

References

[1] Ashurst, W. T. & Meiron, D. I. (1986). Numerical study of vortex reconnection. *Phys. Rev. Lett.*, 58, 1632–1635.

[2] Batchelor, G. K. (1970). *An introduction to Fluid Dynamics*. Cambridge University Press.

[3] Bayly, B. J. (1986). Three-dimensional instability of elliptic flow. *Phys. Rev. Lett.*, 57, 2160–2064.

[4] Betchov, R. (1976). On the non-gaussian aspects of turbulence. *Archiv of Mechanics, Archiwum Mechaniki Stosowanej*, 28, 837–845.

[5] Brachet, M. E., Meiron, D. I., Orszag, S. A., Nickel, B. G., Morf, R. H., & Frisch, U. (1983). Small-scale structure of the taylor-green vortex. *J. Fluid Mech.*, 130, 411–452.

[6] Brenner, M. P., Hormoz, S., & Pumir, A. (2016). Potential singularity mechanism for the euler equations. *Phys. Rev. Fluids*, 1(8), 084503.

[7] Brenner, M. P., Shi, X., & Nagel, S. R. (1994). Iterated instabilities during droplet fission. *Phys. Rev. Lett.*, 73(25), 3391.

[8] Chapman, D. R. (1979). Computational aerodynamics development and outlook. *AIAA Journal*, 17, 1293–1313.

[9] Constantin, P. (2007). On the Euler equations of incompressible fluids. *Bulletin of the American Mathematical Society*, 44(4), 603–621.

[10] Crow, S. C. (1970). Stability theory for a pair of trailing vortices. *AIAA journal*, 8(12), 2172–2179.

[11] Cuypers, Y., Maurel, A., & Petitjeans, P. (2003). Vortex brust as a source of turbulence. *Phys. Rev. Lett.*, 91, 194502.

[12] Darrigol, O. (2002). Between hydrodynamics and elasticity theory: the first five births of the navier-stokes equation. *Archive for History of Exact Sciences*, 56(2), 95–150.

[13] Douady, S., Couder, Y., & Brachet, M. (1991). Direct observation of the intermittency of intense vorticity filaments in turbulence. *Physical Review Letters*, 67(8), 983.

[14] Falkovich, G. & Sreenivasan, K. R. (2006). Lessons from hydrodynamic turbulence. *Phys. Today*, 4(4), 43.

[15] Fefferman, C. L. (2006). Existence and smoothness of the Navier-Stokes equation. *The Millennium Prize problems*, (pp. 57–67).

[16] Frisch, U. (1995). *Turbulence: the legacy of AN Kolmogorov*. Cambridge University Press.

[17] Gendron, P.-O., Avaltroni, F., & Wilkinson, K. (2008). Diffusion coefficients of several rhodamine derivatives as determined by pulsed field gradient–nuclear magnetic resonance and fluorescence correlation spectroscopy. *Journal of fluorescence*, 18(6), 1093.

[18] Gharib, M., Rambod, E., & Shariff, K. (1998). A universal time scale for vortex ring formation. *Journal of Fluid Mechanics*, 360, 121–140.

[19] Goto, S. (2012). Coherent structures and energy cascade in homogeneous turbulence. *Progress of Theoretical Physics Supplement*, 195, 139–156.

[20] Goto, S., Saito, Y., & Kawahara, G. (2017). Hierarchy of antiparallel vortex tubes in spatially periodic turbulence at high reynolds numbers. *Phys. Rev. Fluids*, 2, 064603.

[21] Hormoz, S. & Brenner, M. P. (2012). Absence of singularity of interacting vortex filaments. *J. Fluids Mech.*, 707, 191–204.

[22] Hou, Y. T. & Li, R. (2006). Absence of singular stretching of interacting vortex filaments. *J. Nonlinear Sci.*, 16, 639–664.

[23] Ishihara, T., Gotoh, T., & Kaneda, Y. (2009). Study of high–reynolds number isotropic turbulence by direct numerical simulation. *Annual Review of Fluid Mechanics*, 41, 165–180.

[24] Jiménez, J. (2007). Intermittency in turbulence. In *Proc. 15th "Aha Huliko" a Winter Workshop, Extreme Events* (pp. 81–90).

[25] Jiménez, J., Wray, A. A., Saffman, P. G., & Rogallo, R. S. (1993). The structure of intense vorticity in isotropic turbulence. *Journal of Fluid Mechanics*, 255, 65–90.

[26] Kerr, R. M. (1993a). Evidence for a singularity of the three-dimensional incompressible Euler equations. *Physics of Fluids A*, 5, 1725–1746.

[27] Kerr, R. M. (1993b). Trefoil knot time scales for reconnection and helicity. *Fluid Dynamics Research*, 50, 011422.

[28] Kerr, R. M. (2013). The growth of vorticity moments in the euler equations. *Procedia IUTAM*, 7, 49–58.

[29] Kerswell, R. R. (2002). Elliptical instability. *Annu. Rev. Fluid Mech.*, 34, 83–113.

[30] Keylock, C., Kida, S., & Peters, N. (2016). Jsps supported symposium on interscale transfers and flow topology in equilibrium and non-equilibrium turbulence (sheffield, uk, september 2014). *Fluid Dynamics Research*, 48(2).

[31] Kida, S. & Takaoka, M. (1987). Bridging in vortex reconnection. *Phys. Fluids*, 30, 2911–2914.

[32] Kim, J. & Moin, P. (1985). Application of a fractional-step method to incompressible Navier-Stokes equations. *Journal of Computational Physics*, 59(2), 308–323.

[33] Kleckner, D. & Irvine, W. T. (2013). Creation and dynamics of knotted vortices. *Nature Physics*, 9(4), 253–258.

[34] Kolmogorov, A. N. (1941). The local structure of turbulence in incompressible viscous fluid for very large Reynolds numbers. In *Dokl. Akad. Nauk SSSR*, volume 30 (pp. 299–303).

[35] Laporte, F. & Corjon, A. (2000). Direct numerical simulations of the elliptic instability of a vortex pair. *Phys. Fluids*, 12, 1016–1031.

[36] Lavin, I. (2018). Leonardo's watery chaos. IAS, The Institute Letter, Spring 2018.

[37] Le Dizès, S. & Laporte, F. (2002a). Theoretical predictions for the elliptical instability in a two-vortex flow. *J. Fluid Mech.*, 201, 169–201.

[38] Le Dizès, S. & Laporte, F. (2002b). Theoretical predictions for the elliptical instability in a two-vortex flow. Erratum, private communication.

[39] Leweke, T., Le Dizès, S., & Williamson, C. H. (2016). Dynamics and instabilities of vortex pairs. *Annual Review of Fluid Mechanics*, 48, 507–541.

[40] Leweke, T. & Williamson, C. H. (1998). Cooperative elliptic instability of a vortex pair. *J. Fluid Mech.*, 360, 85–119.

[41] Lim, T. & Nickels, T. (1992). Instability and reconnection in the head-on collision of two vortex rings. *Nature*, 357(6375), 225–227.

[42] Lin, C. C. (1947). Remarks on the spectrum of turbulence. In *Proceedings of the First Symposium of Applied Mathematics*.

[43] Lundgren, T. (1982). Strained spiral vortex model for turbulent fine structure. *Phys. Fluids*, 25, 2193–2203.

[44] McGavin, P. & Pontin, D. I. (2018). Vortex line topology during vortex tube reconnection. *Phys. Rev. Fluids*, 3, 054701.

[45] McKeown, R., Ostilla-Mónico, R., Pumir, A., Brenner, M. P., & Rubinstein, S. M. (2018a). Cascade leading to the emergence of small scale structures in vortex ring collisions. *Phys. Rev. Fluids*, 3(12), 124702.

[46] McKeown, R., Ostilla-Mónico, R., Pumir, A., Brenner, M. P., & Rubinstein, S. M. (2018b). Cascade leading to the emergence of small structures in vortex ring collisions. *Physical Review Fluids*, 3(12), 124702. See Supplemental Material at http://link.aps.org/supplemental/10.1103/PhysRevFluids.3.124702 for supplemental videos.

[47] McKeown, R., Ostilla-Mónico, R., Pumir, A., Brenner, M. P., & Rubinstein, S. M. (2020a). Turbulence generation through an iterative cascade of the elliptical instability. *Science Advances*, 6(9), eaaz2717.

[48] McKeown, R., Ostilla-Mónico, R., Pumir, A., Brenner, M. P., & Rubinstein, S. M. (2020b). Turbulence generation through an iterative cascade of the elliptical instability. *Science Advances*, 6(9), eaaz2717. See Supplemental Material at https://advances.sciencemag.org/content/6/9/eaaz2717/tab-figures-data for supplemental Movies.

[49] Melander, M. V. & Hussain, F. (1989). Cross-linking of two antiparallel vortex tubes. *Phys. Fluids A*, 1, 633–636.

[50] Moffatt, H., Kida, S., & Ohkitani, K. (1994). Stretched vortices–the sinews of turbulence; large-Reynolds-number asymptotics. *Journal of Fluid Mechanics*, 259, 241–264.

[51] Moisy, F. & Jiménez, J. (2004). Geometry and clustering of intense structures in isotropic turbulence. *Journal of fluid mechanics*, 513, 111.

[52] Moore, D. W. & Saffman, P. G. (1972). The motion of a vortex filament with axial flow. *Philos. Trans. R. Soc. London Ser. A*, 272, 403–429.

[53] Moore, D. W. & Saffman, P. G. (1975). The instability of a straight vortex filament in a strain field. *Proceedings of the Royal Society of London. A. Mathematical and Physical Sciences*, 346(1646), 413–425.

[54] Motoori, Y. & Goto, S. (2019). Generation mechanism of a hierarchy of vortices in a turbulent boundary layer. *Journal of Fluid Mechanics*, 865, 1085–1109.

[55] Oshima, Y. (1978). Head-on collision of two vortex rings. *J. Phys. Soc. Japan*, 44, 328–331.

[56] Oshima, Y. & Asaka, S. (1977). Interaction of two vortex rings along parallel axes in air. *J. Phys. Soc. Japan*, 42, 708–713.

[57] Pope, S. B. (2000). *Turbulent flows*. Cambridge University Press.

[58] Pumir, A. & Kerr, R. M. (1987). Numerical simulation of interacting vortex tubes. *Physical Review Letters*, 58(16), 1636.

[59] Pumir, A. & Siggia, E. D. (1987). Vortex dynamics and the existence of solutions to the navier-stokes equations. *Physics of Fluids*, 30, 1606–1626.

[60] Pumir, A. & Siggia, E. D. (1990). Collapsing solutions to the 3-D Euler equations. *Physics of Fluids A*, 2, 220–241.

[61] Reynolds, O. (1883). An experimental investigation of the circumstances which determine whether the motion of water shall be direct or sinuous, and of the law of resistance in parallel channels. *Philosophical Transactions of the Royal society of London*, 174, 935–982.

[62] Reynolds, O. (1895). On the dynamical theory of incompressible viscous fluids and the determination of the criterion. *Phil. Trans. R. Soc. A*, 186(16), 123–164.

[63] Richardson, L. F. (1922). *Weather prediction by numerical process*. Cambridge University Press.

[64] Saffman, P. G. (1990). A model of vortex reconnection. *J. Fluid Mech.*, 212, 395–402.

[65] Saffman, P. G. (1992). *Vortex Dynamics*. Cambridge University Press.

[66] Schaeffer, N. & Le Dizès, S. (2010). Nonlinear dynamics of the elliptic instability. *J. Fluid Mech.*, 646, 471–480.

[67] Schatzle, P. R. (1987). *An experimental study of fusion of vortex rings*. Thesis, California Institute of Technology.

[68] Scheeler, M. W., van Rees, W. M., Kedia, H., Kleckner, D., & Irvine, W. T. (2017). Complete measurement of helicity and its dynamics in vortex tubes. *Science*, 357(6350), 487–491.

[69] Shelley, M., Meiron, D., & Orszag, S. (1993). Dynamical aspects of vortex reconnection of perturbed anti-parallel vortex tubes. *Journal of Fluid Mechanics*, 246, 613–652.

[70] Shi, X., Brenner, M. P., & Nagel, S. R. (1994). A cascade of structure in a drop falling from a faucet. *Science-New York then Washington*, (pp. 219–219).

[71] Siggia, E. D. (1981). Numerical study of small-scale intermittency in three-dimensional turbulence. *J. Fluid Mech.*, 107, 375–406.

[72] Siggia, E. D. (1985). Collapse and amplification of a vortex filament. *Physics of Fluids*, 28, 794–805.

[73] Siggia, E. D. & Pumir, A. (1985). Incipient singularities in the navier-stokes equations. *Phys. Rev. Lett.*, 55, 1749–1752.

[74] Tao, T. (2016). Finite time blowup for an averaged three-dimensional Navier-Stokes equation. *Journal of the American Mathematical Society*, 29(3), 601–674.

[75] Taylor, G. I. (1935). Statistical theory of turbulence. ii. *Proc. Roy. Soc. A*, 151, 444–454.

[76] Taylor, G. I. & Green, A. E. (1937). Mechanism of the production of small eddies from large ones. *Proc. Roy. Soc. A*, 158, 499–521.

[77] Taylor, G. I. & Greene, A. E. (1937). Mechanisms of the production of small eddies from the large ones. *Proc. R. Soc. London A*, 158, 499–521.

[78] Tsai, C. Y. & Widnall, S. E. (1976). The stability of short waves on a straight vortex filament in a weak externally imposed strain field. *Journal of Fluid Mechanics*, 73(4), 721–733.

[79] van der Poel, E. P., Ostilla-Mónico, R., Donners, J., & Verzicco, R. (2015). A pencil distributed finite difference code for strongly turbulent wall-bounded flows. *Computers & Fluids*, 116, 10–16.

[80] Verzicco, R. & Orlandi, P. (1996). A finite-difference scheme for three-dimensional incompressible flows in cylindrical coordinates. *Journal of Computational Physics*, 123(2), 402–414.

[81] Waleffe, F. (1990). On the threedimensionality of strained vortices. *Phys. Fluids A*, 2, 76–80.

THIS THESIS WAS TYPESET using LaTeX, originally developed by Leslie Lamport and based on Donald Knuth's TeX. The body text is set in 11 point Egenolff-Berner Garamond, a revival of Claude Garamont's humanist typeface. The above illustration, "Science Experiment 02", was created by Ben Schlitter and released under CC BY-NC-ND 3.0. A template that can be used to format a PhD thesis with this look and feel has been released under the permissive MIT (X11) license, and can be found online at github.com/suchow/Dissertate or from its author, Jordan Suchow, at suchow@post.harvard.edu.